Journal of Chemistry

Composite Nanoparticles

Guest Editors: Pietro Calandra, Valeria La Parola, Vincenzo Turco Liveri, Elefterios Lidorikis, and Fabio Finocchi

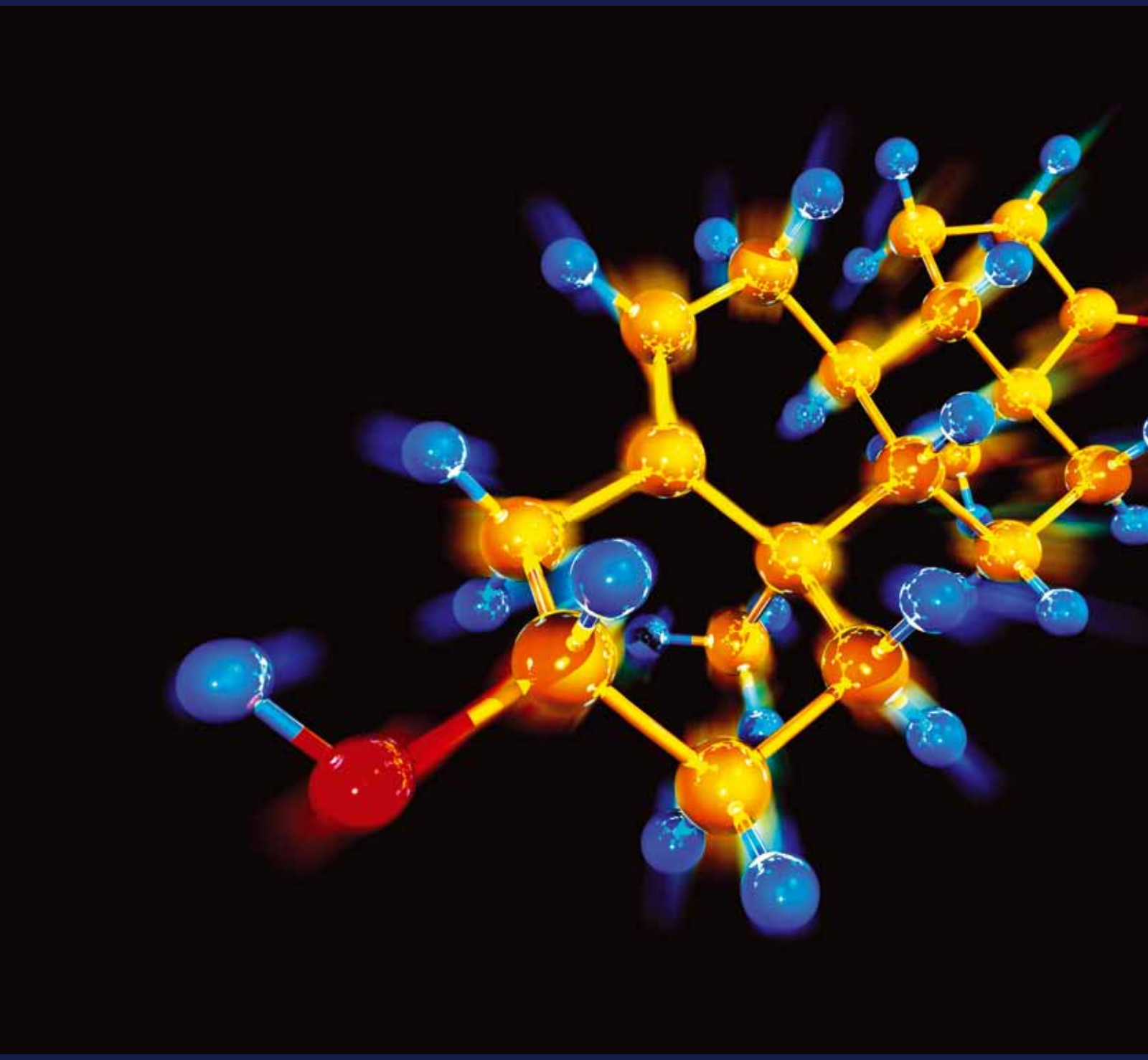

Composite Nanoparticles

Journal of Chemistry

Composite Nanoparticles

Guest Editors: Pietro Calandra, Valeria La Parola, Vincenzo Turco Liveri, Elefterios Lidorikis, and Fabio Finocchi

Contents

Hindawi Publishing Corporation
Journal of Chemistry
Volume 2013, Article ID 536341, 2 pages
http://dx.doi.org/10.1155/2013/536341

Editorial
Composite Nanoparticles

Pietro Calandra,[1] Valeria La Parola,[2] Vincenzo Turco Liveri,[3] Elefterios Lidorikis,[4] and Fabio Finocchi[5]

[1] *CNR-IPCF, National Council of Research, Institute for Physico-Chemical Processes, Viale Ferdinando Stagno d'Alcontres, 98158 Messina, Italy*
[2] *Institute of Nanostructured Materials (ISMN-CNR UOS Palermo), Via Ugo La Malfa 153, 90146 Palermo, Italy*
[3] *Dipartimento di Scienze e Tecnologie Biologiche Chimiche e Farmaceutiche (STEBICEF), Università Degli Studi di Palermo, Viale delle Scienze, Edificio 17, 90128 Palermo, Italy*
[4] *Department of Materials Science and Engineering, University of Ioannina, 45110 Ioannina, Greece*
[5] *Institute of Nanoscience of Paris (INSP), CNRS and University Paris 6, Paris, France*

Correspondence should be addressed to Pietro Calandra; calandra@me.cnr.it

Received 28 May 2013; Accepted 28 May 2013

Composite nanoparticles are advanced materials having recently gained increasing attention due to their scientific and technological importance. They find a wide variety of applications such as catalysts with huge activity and specificity, metal semiconductor junctions, optical sensors, and modifiers of polymeric films for packaging.

From a scientific point of view the composition and the atomic order of the aggregates, in addition to size, are pivotal factors in determining their properties and functionalities, while the nanoscale regime confers to them structural and electronic degrees of freedom which are inaccessible to bulk materials.

The first indispensable stage to develop novel nanotechnologies is the preparation of tailored composite nanostructures. Virtually all the possible physicochemical phenomena have been employed to reach this objective allowing to set up a huge number of protocols each one with its specific advantages and disadvantages. The aspects of novel preparation methods are addressed in two manuscripts.

S. Bagheri et al. describe a novel synthesis of anatase titanium dioxide nanoparticles using egg white solution via sol-gel method and characterized them through a high number of techniques. The main advantage of using egg white proteins as a gelling agent is that it can provide long-term stability for nanoparticles by preventing particles agglomeration. They demonstrated that egg white solution is a reliable and cheap green gelling agent that can be used as a matrix in the sol-gel method to synthesise tiny size TNPs.

V. Ovchinnikov and A. Shevchenko describe a cost-effective fabrication of random noble-metal nanostructures with a feature size of the order of 10 nm on a large-area dielectric substrate. The technique allows to create metal nanoislands on a nanopatterned dielectric template with an enhanced adhesion between the metal and the dielectric. The use of the adhesion layer (that makes the structures stable) is important in view of variety of optical and other potential applications of the structures. The results of their work can be of interest in regard to the development of new approaches to self-organization based nanofabrication of extremely small metal and metal-dielectric nanostructures on large-area substrates.

Due to their peculiarities, the production of nanomaterials is a promising strategy to fuel novel technological applications. Two manuscripts, highlighting enhanced properties for applicative purposes, are good examples of the potentialities of these materials.

M. C. Carrera et al. studied the permeation of CO_2 in films of high density polyethylene (HDPE) and organoclay modified with polyvinylalcohol ($MMT_{HDTMA/PVA}$) obtained from melt blending. They showed that the incorporation of the modified organoclay generated an exfoliated nanocomposite structure with a significant effect on the barrier

properties of HDPE. Notably the mechanical properties remain equal to those of pure polyethylene, but with an increase in barrier properties to CO_2 allowing to obtain nanocomposites of HDPE competitively used in packaging.

Q. X. Li et al. prepared a novel Pd/C catalyst with enhanced performance for direct ethanol fuel cell. They characterized the catalysts by XRD and TEM showing that they are spherical and homogeneously dispersed on carbon.

Finally, the theoretical/computational approach has been faced by P. Shabanzadeh et al. In their investigation, they applied the accuracy of artificial neural network training algorithm to study the effects of different parameters on the synthesis of Ag nanoparticles performed in the interlamellar space of montmorillonite (MMT) by chemical reduction technique. Using the best performing artificial neural network, they predicted the optimum conditions of $AgNO_3$ concentration, MMT d-spacing, and reaction temperature.

By compiling these papers, we hope to enrich our readers and researchers with respect to the most recent progresses in the field of nanoscale multicomponent particles.

Pietro Calandra
Valeria La Parola
Vincenzo Turco Liveri
Elefterios Lidorikis
Fabio Finocchi

Hindawi Publishing Corporation
Journal of Chemistry
Volume 2013, Article ID 305713, 8 pages
http://dx.doi.org/10.1155/2013/305713

Research Article

Artificial Intelligence in Numerical Modeling of Silver Nanoparticles Prepared in Montmorillonite Interlayer Space

Parvaneh Shabanzadeh,[1] Norazak Senu,[1] Kamyar Shameli,[2,3] and Maryam Mohaghegh Tabar[4]

[1] *Department of Mathematics, Faculty of Science, Universiti Putra Malaysia, 43400 Serdang, Selangor, Malaysia*
[2] *Department of Chemistry, Faculty of Science, Universiti Putra Malaysia, 43400 Serdang, Selangor, Malaysia*
[3] *Nanotechnology and Advance Materials Department, Materials & Energy Research Center, Alborz, Karaj 31787/316, Iran*
[4] *Department of Mathematics, Faculty of Science, University of Gilan, Rasht 1914, Iran*

Correspondence should be addressed to Parvaneh Shabanzadeh; parvaneh.shabanzade@gmail.com

Received 14 December 2012; Revised 29 January 2013; Accepted 10 February 2013

Academic Editor: Elefterios Lidorikis

Artificial neural network (ANN) models have the capacity to eliminate the need for expensive experimental investigation in various areas of manufacturing processes, including the casting methods. An understanding of the interrelationships between input variables is essential for interpreting the sensitivity data and optimizing the design parameters. Silver nanoparticles (Ag-NPs) have attracted considerable attention for chemical, physical, and medical applications due to their exceptional properties. The nanocrystal silver was synthesized into an interlamellar space of montmorillonite by using the chemical reduction technique. The method has an advantage of size control which is essential in nanometals synthesis. Silver nanoparticles with nanosize and devoid of aggregation are favorable for several properties. In this investigation, the accuracy of artificial neural network training algorithm was applied in studying the effects of different parameters on the particles, including the $AgNO_3$ concentration, reaction temperature, UV-visible wavelength, and montmorillonite (MMT) d-spacing on the prediction of size of silver nanoparticles. Analysis of the variance showed that the $AgNO_3$ concentration and temperature were the most significant factors affecting the size of silver nanoparticles. Using the best performing artificial neural network, the optimum conditions predicted were a concentration of $AgNO_3$ of 1.0 (M), MMT d-spacing of 1.27 nm, reaction temperature of 27°C, and wavelength of 397.50 nm.

1. Introduction

Nanoparticles are important materials for fundamental studies and diversified technical applications because of their size dependent properties or highly active performance due to their large surface areas. The synthesis of well dispersed pure metal nanoparticle is difficult as they have high tendency to form agglomerates particles [1, 2]. Therefore, to overcome agglomeration, preparation of nanoparticles based on clay compounds in which nanoparticles are supported within the interlamellar spaces of clay and/or on its external surfaces is one of the most effective solutions [3, 4]. In the same way, synthesis of metal nanoparticle on solid supports such as smectite clays is also a suitable way to prepare practically applicable supported particles as well as to control the particle size [5].

Smectite clays have an excellent swelling and adsorption ability, which is especially interesting for the impregnation of antibacterial active nanosize metals in the interlamellar space of clay [6, 7]. Montmorillonite (MMT) as lamellar clay has intercalation, swelling, and ion exchange properties. Its interlayer space has been used for the synthesis of material and biomaterial nanoparticles [8].

Due to its properties and areas of use, Ag is one of the most studied metals. However, certain factors, such as stability, morphology, particle size distribution, and surface state charge/modification which are significant in the controlled synthesis of Ag-NPs have attracted high attention, since this

task is far from being understood [5–8]. For the synthesis of Ag-NPs in the solid substrate, $AgNO_3$ is often used as the primary source of Ag^+. There are numerous ways of Ag^+ reduction: use of γ-ray [4], or UV irradiations [5], glucose [2], application of reducing chemicals, such as hydrazine [9], sodium borohydride [1, 3, 6–8], plant extraction [10, 11], and so forth.

Artificial neural network (ANN) is a nonlinear statistical analysis technique and is especially suitable for simulation of systems which are hard to be described by physical and chemical models. It provides a way of linking input data to output data using a set of nonlinear functions [12]. The ANN is a highly simplified model of the structure of a biological network [13]. The fundamental processing element of ANN is an artificial neuron or simply a neuron. A biological neuron receives inputs from other sources, combines them, performs generally a nonlinear operation on the result, and then outputs the final result [14]. The basic advantage of ANN is that it does not need any mathematical model since an ANN learns from examples and recognizes patterns in a series of input and output data without any prior assumptions about their nature and interrelations [13]. The ANN eliminates the limitations of the classical approaches by extracting the desired information using the input data. Applying ANN to a system needs sufficient input and output data instead of a mathematical equation [15].

Selecting the optimum architecture of the network is one of the challenging steps in ANN modelling. The term "architecture" mentions the number of layers in the network and number of neurons in each layer. Also a training algorithm is required for solving a problem via a neural network modeling. Many different algorithms can be applied for training procedure. During the training process, the weights and biases in the network are modified to minimize the error and obtain a high performance in the solution. At the end of the training and during the training error, mean absolute percentage error is computed between desired outputs and target outputs [16, 17]. It is the most useful numerical technique in modern engineering analysis and has been employed to study different problems in heat transfer, electrical systems, mechanical properties, solid mechanics, rigid body dynamics, fluid mechanics, and many other fields. In recent years, ANN has been introduced in nanotechnology applications as techniques to model data showing nonlinear relationships [12, 17–20] and/or estimation of particle size in variety of nanoparticle samples [21].

Employing neural network models would lead to saving time and cost by predicting the results of the reactions so that the most promising conditions can then be verified [22].

The aim of the present research is the investigation of the effects of different parameters including $AgNO_3$ concentration, temperature, wavelength, and MMT interlayer d-spacing on the prediction of size of Ag-NPs. The ANN model was used to predict the optimum size of Ag-NPs.

2. Experimental

To prepare the stable Ag-NPs via the chemical reduction method, it was significant to choose the suitable stabilizer and reducing agent. In this research, MMT suspension was used as the appropriate support for reducing $AgNO_3$/MMT suspension using $NaBH_4$ as the strong reducing agent. The surfaces of MMT suspension are assisting the Ag-NPs nucleation during the reduction process. The schematic illustration of the synthesis of Ag/MMT nanocomposites from $AgNO_3$/MMT suspension produced by using sodium borohydride is shown in Figure 1. Meanwhile, as shown in (Figure 1(a)) $AgNO_3$/MMT suspension was colourless, but after the addition of the reducing agent to the suspension they turned to brown colour indicating the formation of Ag-NPs in the MMT suspensions (Figure 1(b)).

2.1. Data Sets. Table 1 shows the experimental data used for ANN design. The experimental data were randomly divided into three sets: 26, 10, and 6, which were used as training, validation, and testing, respectively. The training data was applied to compute the network parameters while the validation data was applied to ensure robustness of the network parameters. If a network "learns too well" from the training data, the rules might not fit as well for the rest of the cases in the data. To avoid this "over fitting" phenomenon, the testing stage was used to control error; when it increased, the training stops [23]. For assessment the predictive ability of the generated model was used as the testing data set.

2.2. ANN Description. An artificial neural network learns general rules based on calculation upon numerical data [24]. Neurons are the smallest parts of ANN. Neurons are constructed in three layers including input, output, and hidden layer. The hidden layer can be developed with similar layer structure as neuron. In the other expression, the structure is as if the output of a hidden layer is the input for the sequent hidden layer [25]. The multilayer perceptron (MLP) networks are the most widely used neural networks that consist of one input layer, one output layer, and one or more hidden layers. In the ANN methodology, the sample data is often subdivided into training, validation, and test sets. The distinctions among these subsets are crucial. Ripley [26] defines the following "Training set: A set of examples used for learning that is to fit the parameters (weights) of the classifier. Validation set: A set of examples used to tune the parameters of a classifier, for example, to choose the number of hidden units in a neural network. Test set: A set of examples used only to assess the performance (generalization) of a fully specified classifier." In this research, a multilayer perception (MLP) based feed forward ANN which uses back-propagation learning algorithm, was applied for the modeling of Ag-NPs size prediction. The inputs for the network include $AgNO_3$ concentration, reaction temperature, UV-visible wavelength, and MMT d-spacing. The output is the size of Ag-NPs. In Figure 2, is shown a diagram of a typical MLP neural network with one hidden layer structure of proposed ANN. The input to the node l in the hidden layer is given by

$$\partial_l = \sum_{i=1}^{q} \left(X_i W_{il}\right) + \theta_l \quad l = 1, 2, \ldots, s. \tag{1}$$

Each neuron consists of a transfer function expressing an internal activation level. The output from a neuron is

Table 1: Experimental values (training, validation, and testing data set), actual and model predicated of size of Ag-NPs.

No.	$AgNO_3$ con. (M)	Temperature (°C)	Wavelength (nm)	MMT d-spacing (nm)	Size of Ag-NPs (actual)	Size of Ag-NPs (predict)
			Training set			
1	0.5	30	397	1.25	3.85	3.84
2	0.5	35	398	1.25	3.84	3.85
3	0.5	50	398	1.26	3.87	3.88
4	0.5	60	399	1.27	3.89	3.88
5	1	30	398	1.26	4.2	4.20
6	1	35	399	1.26	4.21	4.22
7	1	50	401	1.28	4.24	4.23
8	1	60	403	1.29	4.24	4.24
9	1.5	30	402	1.26	4.68	4.68
10	1.5	35	403	1.28	4.69	4.68
11	1.5	50	405	1.35	4.71	4.72
12	1.5	60	406	1.38	4.93	4.93
13	2	30	403	1.33	6.74	6.74
14	2	35	404	1.35	6.75	6.75
15	2	50	406	1.41	6.88	6.87
16	2	60	407	1.44	6.95	6.95
17	5	30	406	1.47	8.54	8.55
18	5	35	408	1.47	8.56	8.55
19	5	50	411	1.52	8.63	8.63
20	5	60	418	1.55	8.71	8.71
			Validation set			
21	0.5	40	398	1.26	3.86	3.85
22	1	25	398	1.25	4.19	4.11
23	1.5	25	400	1.26	4.67	4.75
24	1.5	40	404	1.32	4.69	4.67
25	2	40	405	1.37	6.79	6.74
26	5	25	406	1.47	8.53	8.51
			Testing set			
27	0.5	25	396	1.24	3.82	3.84
28	1	40	399	1.28	4.22	4.24
29	2	25	402	1.31	5.08	6.66
30	5	40	408	1.49	8.56	8.55

Concentration (con.), molar (M), degree centigrade (°C), nanometre (nm), montmorillonite (MMT), silver nanoparticles (Ag-NPs).

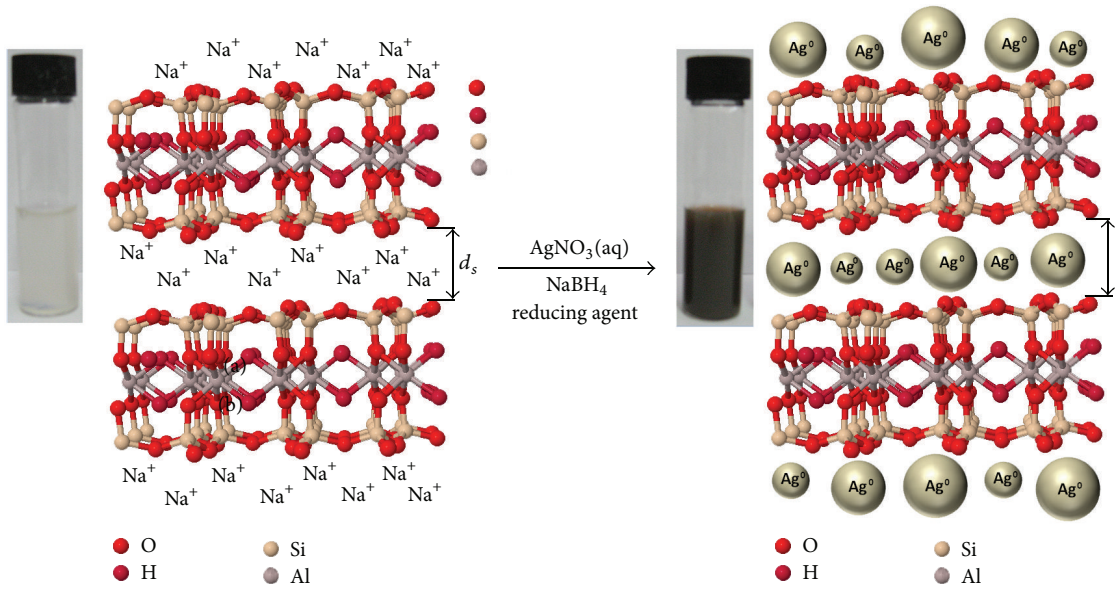

Figure 1: Schematic illustration of the synthesized Ag-NPs in the interlayer space of MMT suspension by chemical reduction method.

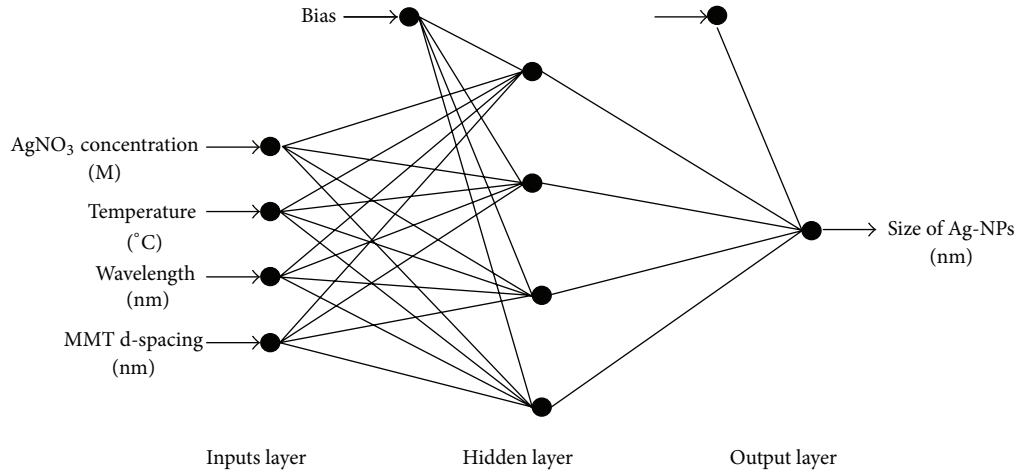

Figure 2: Schematic diagram of MLP neural network.

determined by transforming its input using a suitable transfer function [27]. Generally, the transfer functions for function approximation (regression) are sigmoidal function, hyperbolic tangent, and linear function [28]. The most popular transfer function for a nonlinear relationship is the sigmoidal function [19, 29]. The output from l the neuron of the hidden layer is given by

$$O_l = f\left(\partial_l\right). \tag{2}$$

In (1) and (2), q is the number of neurons in the input layer, s is the number of neurons in the hidden layer, θ_l is the bias term, w is the weighting factor, and f is the activation function of the hidden layer such as the tan-sigmoid transfer function [18, 30].

The output of the jth neuron in the output layer is given by

$$Y_j = \sum_{i=1}^{s}\left(O_i W_{ij}\right) + b_j \qquad j = 1, 2, \ldots, m, \tag{3}$$

where W is the weighting factor, b is the bias term, and m is the number of neurons in the output layer. The values of the interconnection weights are determined by the training or learning process using a set of data. The aim is to find the value of the weight that minimizes the error [28]. A popular measure for evaluation of prediction ability of ANN models is the root mean square error (RMSE):

$$\mathrm{RMSE} = \left(\frac{1}{r}\sum_{i=1}^{r}\left(x_{pi} - x_{ai}\right)^2\right)^{1/2}, \tag{4}$$

where r is the number of points, x_{pi} is the predicted value obtained from the neural network model, and x_{ai} is the actual value. The coefficient of determination R^2 reflects the degree of fit for the mathematical model [31]. The closer the R^2 value is to 1, the better the model fitting towards the actual data [32]:

$$R^2 = 1 - \frac{\sum_{i=1}^{r}\left(x_{pi} - x_{ai}\right)^2}{\sum_{i=1}^{r}\left(x_{ai} - x_m\right)^2}, \tag{5}$$

where r is the number of points, x_{pi} is the predicted value obtained from the neural network model, x_{ai} is the actual value, and x_m is the average of the actual values. Absolute average deviation (AAD) is another important index to evaluate the ANN output error between the actual and the predicted output [14]:

$$\mathrm{AAD} = \left\{\frac{\left[\sum_{i=1}^{r}\left(\left|x_{pi} - x_{ai}\right| / x_{ai}\right)\right]}{r}\right\} \times 100, \tag{6}$$

where x_{pi} and x_{ai} are the predicted and actual responses, respectively, and r is the number of the points. The network having minimum RMSE, minimum AAD, and maximum R^2 is considered as the best neural network model [33].

3. Results and Discussion

3.1. ANN Modeling Results. In this research, many different structures with two and three hidden layers with the different number of neurons in each layer were tested to obtain the best ANN configuration. The choosing of number of neurons in hidden layers is very important as it affects the training time and generalization property of neural networks. A higher value of neurons in hidden layer may force the network to memorize (as opposed to generalize) the patterns which it has seen during training whereas a lower value of neurons in hidden layer would waste a great deal of training time in finding its optimal representation [34]. There is no general rule for selecting the number of neurons in a hidden layer. It depends on the complexity of the system being modeled [33]. The most popular approach for finding the optimal number of neurons in hidden layer is by trial and error [35]. The tan-sigmoid function is used as transfer function for first layer and linear function is applied as transfer function for second layer.

In this paper, the trial and error approach was utilized in determining the optimum neurons in the hidden layers. The feed-forward neural network generally has one or more hidden layers, which enable the network to model nonlinear and complex functions [28]. Nevertheless, the number of

Table 2: Values of connection weights (parameters of the model) for the completed ANN model.

	Node 1	Node 2	Node 3	Node 4	Bias 2
Input 1	−1.4013	0.9907	−3.3446	0.3431	—
Input 2	1.4975	1.6411	−0.1142	0.7898	—
Input 3	−2.0753	−0.3112	0.1400	2.0698	—
Input 4	−0.3952	−1.4632	−2.9757	0.3286	—
Bias 1	4.0921	−0.8315	−1.7845	3.2889	—
Output	−1.7714	−0.21919	−0.6525	0.16557	1.4701

hidden layers is difficult to decide [19]. It has been reported in the literature that one hidden layer is normally sufficient to provide an accurate prediction and can be the first choice for any practical feed-forward network design [36].

Therefore, a single hidden layer network was applied in this paper [12, 20]. The RMSE was applied as the error function. Also, R^2 and AAD were used as a measure of the predictive ability of the network. Each topology was repeated five times to avoid random correlation due to the random initialization of the weights [37]. Many types of learning algorithms are explained in the literature which can be applied for training of the network. However, it is difficult to know which learning algorithm will be more efficient for a given problem [38].

The LM is often the fastest back-propagation algorithm and is highly recommended as a first-choice supervised algorithm, even though it does require more memory than other algorithms. The LM back-propagation is a network training function that updates weight and bias values according to LM optimization. The LM is an approximation to the Newton's method [39]. This is very well suited to the training of the neural network [40]. The algorithm uses the second-order derivatives of the mean squared error between the desired output and the actual output so that better convergence behavior can be obtained [41]. Therefore, various topologies (from 1 to 20 hidden neurons) using LM algorithm were examined. Results obtained showed that a network with 4 hidden neurons presented the best performance.

Figure 3 presents the scatter plots of the ANN model predicted versus actual values using LM algorithm for the training, validation, testing, and all data sets. Also, it presents the predicted model for the training, validation, testing, and all data sets well fitted to the actual values. The results of this study illustrated that the network consisted of three layers: input, hidden, and output with 4 nodes in hidden layer presenting the best performances. RMSE and R^2 between the actual and predicted values were determined as 0.0055 and 0.9999 for training set, 0.01529 and 0.9994 for validation set, and 0.7917 and 0.955 for testing set. The RMSE and R^2 for all data sets were also calculated as 0.0071 and 0.9753, respectively. These results show that the predictive accuracy of the model is high. In Table 2 are showed values of connection weights (parameters of the model) for the completed ANN model.

Table 3: Performance evaluation of interactions of input variables for the LM with 4 neurons in the hidden layer for sensitivity analysis.

No.	Combination	RMSE	R^2	AAD
Group of one variable				
1	X_1	0.301	0.985	0.972
2	X_2	0.505	0.085	0.007
3	X_3	0.801	0.893	0.805
4	X_4	1.810	0.960	0.922
Group of two variables				
5	$X_1 + X_2$	0.011	0.993	0.987
6	$X_1 + X_3$	0.015	0.999	0.999
7	$X_1 + X_4$	0.202	0.999	0.999
8	$X_2 + X_3$	0.257	0.989	0.979
9	$X_2 + X_4$	0.251	0.993	0.999
10	$X_3 + X_4$	0.354	0.856	0.888
Group of three variables				
11	$X_1 + X_2 + X_3$	0.009	0.999	0.999
12	$X_1 + X_2 + X_4$	0.240	0.891	0.882
13	$X_1 + X_3 + X_4$	0.046	0.999	0.999
14	$X_2 + X_3 + X_4$	0.013	0.999	0.999
Group of four variables				
15	$X_1 + X_2 + X_3 + X_4$	0.007	0.974	0.999

3.2. Sensitivity Analysis. In this research, a data analysis was performed to determine the effectiveness of a variable using the suggested ANN model in this work [20]. In the analysis, performance evaluations of different possible interaction of variables were investigated. Therefore, performances of the four groups (one, two, three, and four) variables were studied by the optimal ANN model using the LM with 4 neurons in the hidden layer.

The groups of input vectors were defined as follows: X_1, $AgNO_3$ concentration; X_2, reaction temperature; X_3, UV-visible wavelength; and X_4, MMT d-spacing. The results are summarized in Table 3. The results in Table 3 showed X_1 to be the most effective parameter in the group of one variable, due to its lower RMSE, 0.301.

As shown in Table 3, the value of RMSE significantly decreased when X_1 was used in interaction with other variables in other groups. The minimum value of RMSE in the group of two was determined to be 0.011 with a further interaction of X_2. The values of RMSE became smaller in the interaction of $X_1 + X_2$; the best case of group of two variables was used with X_2. The minimum value of RMSE in the group of three variables was 0.009 using the interaction of $X_1 + X_2 + X_3$. The value of RMSE was decreased from 0.009 to 0.007 when X_4 was used in interaction with other variables in the after group of four variables.

3.3. Comparison of Experimental Data and ANN Output. The optimal conditions for the prediction of size of Ag-NPs were predicted as presented in Table 4 along with predicted and actual size of Ag-NPs. For this goal, ANN based LM was adopted for predicting the size of Ag-NPs in optimal conditions and then experiment was carried out under the

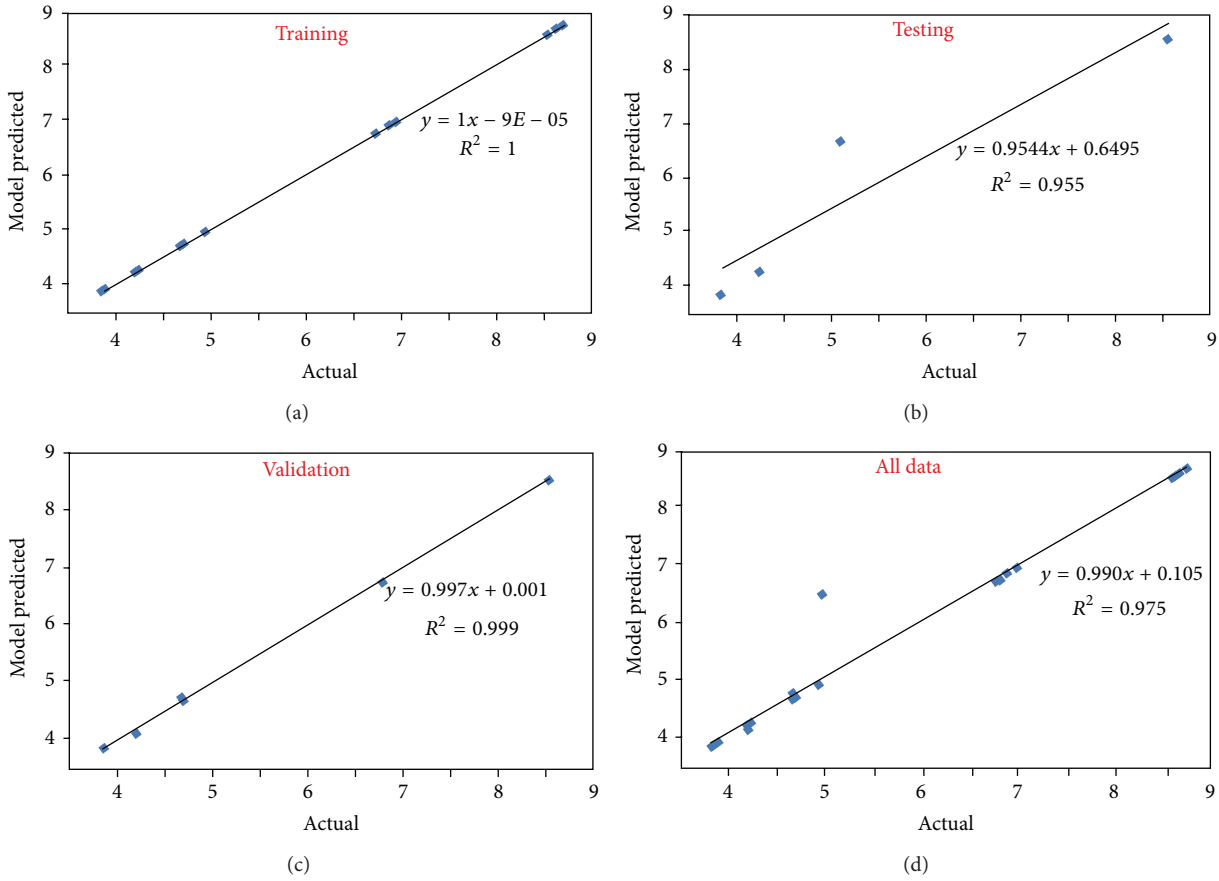

Figure 3: The scatter plots of ANN model predicted versus actual values for training, validation, testing, and all data sets.

Table 4: Optimum conditions derived by ANN for the prediction of size of Ag-NPs.

Optimal conditions				Size of Ag-NPs		
Concentration of $AgNO_3$ (M)	Reaction temperature (°C)	Wavelength (nm)	MMT (d_s) (nm)	Actual	Predicted	Standard deviation
1	27	397.5	1.27	4.3	4.5	0.3

recommended conditions [42]. The resulting response was compared to the predicted value. The optimum parameters were 1 M, 27°C, 397.5 nm, 1.27 nm for the concentration of $AgNO_3$, reaction temperature, UV-visible wavelength, and MMT d-spacing, respectively. As shown in Table 4, the concentration was the most effective parameter on the size of Ag-NPs. The experimental reaction gave a reasonable size of Ag-NPs 4.3 nm. This result confirmed the validity of the model, and the experimental value was determined to be quite close to the ANN predicted value 4.5 nm, less of 1% in relative deviation, implying that the empirical model derived from the ANN can be used to sufficiently describe the relationship between the independent variables and response.

4. Conclusion

In this research, the artificial neural network models for the size prediction of Ag-NPs were presented. The analysis carried out confirms that ANN was a powerful tool for analysis and modeling. Based on the obtained results it can be concluded that the LM neural network model with 4 neurons in 1 hidden layer will be the fastest training algorithm and can present a very good performance for ANN modeling of nanocomposites behaviours. Data analysis showed that $AgNO_3$ concentration (1.0 M) and reaction temperatures (27°C) are two most sensitive parameters. Therefore, employing neural network models would lead to saving time and cost by predicting the results of the reactions.

References

[1] K. Shameli, M. B. Ahmad, M. Zargar, W. M. Z. W. Yunus, and N. A. Ibrahim, "Fabrication of silver nanoparticles doped in the zeolite framework and antibacterial activity," *International Journal of Nanomedicine*, vol. 6, pp. 331–341, 2011.

[2] K. Shameli, M. B. Ahmad, S. D. Jazayeri et al., "Synthesis and characterization of polyethylene glycol mediated silver nanoparticles by the green method," *International Journal of Molecular Sciences*, vol. 13, no. 6, pp. 6639–6650, 2012.

[3] K. Shameli, M. B. Ahmad, W. M. Z. W. Yunus, N. A. Ibrahim, A. Rustaiyan, and M. Zargar, "Synthesis of silver nanoparticles in montmorillonite and their antibacterial behavior," *International Journal of Nanomedicine*, vol. 6, pp. 581–590, 2010.

[4] K. Shameli, M. B. Ahmad, W. M. Z. W. Yunus, N. A. Ibrahim, Y. Gharayebi, and S. Sedaghat, "Synthesis of silver/mont\-morillonite nanocomposites using γ-irradiation," *International Journal of Nanomedicine*, vol. 5, no. 1, pp. 1067–1077, 2010.

[5] K. Shameli, M. B. Ahmad, W. M. Z. W. Yunus et al., "Green synthesis of silver/montmorillonite/chitosan bionanocomposites using the UV irradiation method and evaluation of antibacterial activity," *International Journal of Nanomedicine*, vol. 5, no. 1, pp. 875–887, 2010.

[6] M. B. Ahmad, K. Shameli, W. M. Z. W. Yunus, and N. A. Ibrahim, "Synthesis and characterization of silver/clay/starch bionanocomposites by green method," *The Australian Journal of Basic and Applied Sciences*, vol. 4, no. 7, pp. 2158–2165, 2010.

[7] K. Shameli, M. B. Ahmad, W. M. Z. W. Yunus, N. A. Ibrahim, and M. Darroudi, "Synthesis and characterization of silver/talc nanocomposites using the wet chemical reduction method," *International Journal of Nanomedicine*, vol. 5, pp. 743–751, 2010.

[8] K. Shameli, M. B. Ahmad, M. Zargar et al., "Synthesis and characterization of silver/montmorillonite/chitosan bionanocomposites by chemical reduction method and their antibacterial activity," *International Journal of Nanomedicine*, vol. 6, pp. 271–284, 2011.

[9] K. Szczepanowicz, J. Stefan'ska, R. P. Socha, and P. Warszyn'ski, "Preparation of silver nanoparticles via chemical reduction and their antimicrobial activity," *Physicochemical Problems of Mineral Processing*, vol. 45, pp. 85–98, 2010.

[10] M. Zargar, A. A. Hamid, F. A. Bakar et al., "Green synthesis and antibacterial effect of silver nanoparticles using *Vitex Negundo* L," *Molecules*, vol. 16, no. 8, pp. 6667–6676, 2011.

[11] K. Shameli, M. B. Ahmad, A. Zamanian et al., "Green biosynthesis of silver nanoparticles using *Curcuma longa* tuber powder," *International Journal of Nanomedicine*, vol. 7, pp. 5603–5610, 2012.

[12] M. O. Shabani and A. Mazahery, "Artificial Intelligence in numerical modeling of nano sized ceramic particulates reinforced metal matrix composites," *Applied Mathematical Modelling*, vol. 36, no. 11, pp. 5455–5465, 2011.

[13] S. Mandal, P. V. Sivaprasad, S. Venugopal, and K. P. N. Murthy, "Artificial neural network modeling to evaluate and predict the deformation behavior of stainless steel type AISI 304L during hot torsion," *Applied Soft Computing Journal*, vol. 9, no. 1, pp. 237–244, 2009.

[14] D. Bas and I. H. Bonyaci, "Modeling and optimization II: comparison of estimation capabilities of response surface methodology with artificial neural networks in a biochemical reaction," *Journal of Food Engineering*, vol. 78, no. 3, pp. 846–854, 2007.

[15] M. A. Akcayol and C. Cinar, "Artificial neural network based modeling of heated catalytic converter performance," *Applied Thermal Engineering*, vol. 25, no. 14-15, pp. 2341–2350, 2005.

[16] M. A. Hussain, M. S. Rahman, and C. W. Ng, "Prediction of pores formation (porosity) in foods during drying: generic models by the use of hybrid neural network," *Journal of Food Engineering*, vol. 51, no. 3, pp. 239–248, 2002.

[17] M. G. Moghaddam, F. B. H. Ahmad, M. Basri, and M. B. A. Rahman, "Artificial neural network modeling studies to predict the yield of enzymatic synthesis of betulinic acid ester," *Electronic Journal of Biotechnology*, vol. 15, no. 3, 2010.

[18] M. Rashidi, M. Hayati, and A. Rezaei, "Application of artificial neural network for prediction of the oxidation behavior of aluminized nano-crystalline nickel," *Materials and Design*, vol. 42, pp. 308–316, 2012.

[19] A. Ghaffari, H. Abdollahi, M. R. Khoshayand, I. S. Bozchalooi, A. Dadgar, and M. Rafiee-Tehrani, "Performance comparison of neural network training algorithms in modeling of bimodal drug delivery," *International Journal of Pharmaceutics*, vol. 327, no. 1-2, pp. 126–138, 2006.

[20] M. Khajeh, M. Ghaffari, and M. Shakeri, "Application of artificial neural network in predicting the extraction yield of essential oils of *Diplotaenia cachrydifolia* by supercritical fluid extraction," *The Journal of Supercritical Fluids*, vol. 69, pp. 91–96, 2012.

[21] A. Amani, P. York, H. Chrystyn, B. J. Clark, and D. Q. Do, "Determination of factors controlling the particle size in nanoemulsions using Artificial Neural Networks," *The European Journal of Pharmaceutical Sciences*, vol. 35, no. 1-2, pp. 42–51, 2008.

[22] M. B. Abdul Rahman, N. Chaibakhsh, M. Basri, A. B. Salleh, and R. N. Abdul Rahman, "Application of artificial neural network for yield prediction of lipase catalyzed synthesis of dioctyl adipate," *Applied Biochemistry and Biotechnology*, vol. 158, no. 3, pp. 722–735, 2009.

[23] X. Song, A. Mitnitski, C. MacKnight, and K. Rockwood, "Assessment of individual risk of death using self-report data: an artificial neural network compared with a frailty index," *Journal of the American Geriatrics Society*, vol. 52, no. 7, pp. 1180–1184, 2004.

[24] F. Hakimiyana and V. Derhami, "Design of quantum dot semiconductor optical amplifier by intelligence methods," *Procedia Computer Science*, vol. 3, pp. 449–452, 2011.

[25] A. H. Mesbahi, D. Semnani, and S. N. Khorasani, "Performance prediction of a specific wear rate in epoxy nanocomposites with various composition content of polytetrafluoroethylen (PTFE), graphite, short carbon fibers (CF) and nano-TiO_2 using adaptive neuro-fuzzy inference system (ANFIS)," *Composites B*, vol. 43, no. 2, pp. 549–558, 2012.

[26] B. D. Ripley, *Pattern Recognition and Neural Networks*, Cambridge University Press, Cambridge, UK, 1996.

[27] M. A. Razavi, A. Mortazavi, and M. Mousavi, "Dynamic modelling of milk ultrafiltration by artificial neural network," *Journal of Membrane Science*, vol. 220, no. 1-2, pp. 47–58, 2003.

[28] E. Jorjani, C. S. Chelgani, and S. H. Mesroghli, "Application of artificial neural networks to predict chemical desulfurization of Tabas coal," *Fuel*, vol. 87, no. 12, pp. 2727–2734, 2008.

[29] J. S. Torrecilla, L. Otero, and P. D. Sanz, "Optimization of an artificial neural network for thermal/pressure food processing: evaluation of training algorithms," *Computers and Electronics in Agriculture*, vol. 56, no. 2, pp. 101–110, 2007.

[30] A. R. Gallant and H. White, "On learning the derivatives of an unknown mapping with multilayer feedforward networks," *Neural Networks*, vol. 5, no. 1, pp. 129–138, 1992.

[31] A. Nath and P. K. Chattopadhyay, "Optimization of oven toasting for improving crispness and other quality attributes of ready to eat potato-soy snack using response surface methodology," *Journal of Food Engineering*, vol. 80, no. 4, pp. 1282–1292, 2007.

[32] H. N. Sin, S. Yusof, N. S. A. Hamid, and R. A. Rahman, "Optimization of enzymatic clarification of sapodilla juice using response surface methodology," *Journal of Food Engineering*, vol. 73, no. 4, pp. 313–319, 2006.

[33] L. Wang, B. Yang, R. Wang, and X. Du, "Extraction of pepsin-soluble collagen from grass carp (*Ctenopharyngodon idella*) skin using an artificial neural network," *Food Chemistry*, vol. 111, no. 3, pp. 683–686, 2008.

[34] M. Hussain, J. S. Bedi, H. Singh, M. Hussain, J. S. Bedi, and H. Singh, "Determining number of neurons in hidden layers for binary error correcting codes," in *Proceedings of Applications of Artificial Neural Networks III*, pp. 1015–1022, Orlando, FL, USA, April 1992.

[35] E. F. Ahmed, "Artificial neural networks for diagnosis and survival prediction in colon cancer," *Molecular Cancer*, vol. 4, article 29, 2005.

[36] D. Hush and B. G. Horne, "Progress in supervised neural networks," *IEEE Signal Processing Magazine*, vol. 10, no. 1, pp. 8–39, 1993.

[37] M. B. Kasiri, H. Aleboyeh, and A. Aleboyeh, "Modeling and optimization of heterogeneous photo-fenton process with response surface methodology and artificial neural networks," *Environmental Science and Technology*, vol. 42, no. 21, pp. 7970–7975, 2008.

[38] Ö. G. Saracoglu, "An artificial neural network approach for the prediction of absorption measurements of an evanescent field fiber sensor," *Sensors*, vol. 8, no. 3, pp. 1585–1594, 2008.

[39] M. T. Hagan and M. B. Menhaj, "Training feedforward networks with the Marquardt algorithm," *IEEE Transactions on Neural Networks*, vol. 5, no. 6, pp. 989–993, 1994.

[40] L. M. Saini and M. K. Soni, "Artificial neural network based peak load forecasting using Levenberg-Marquardt and quasi-Newton methods," *IEE Proceedings Generation, Transmission & Distribution*, vol. 149, no. 5, pp. 578–584, 2002.

[41] A. Gulbag and F. Temurtas, "A study on quantitative classification of binary gas mixture using neural networks and adaptive neuro-fuzzy inference systems," *Sensors and Actuators B*, vol. 115, no. 1, pp. 252–262, 2006.

[42] H. R. F. Masoumi, A. Kassim, M. Basri, D. K. Abdullah, and M. J. Haron, "Multivariate optimization in the biosynthesis of a triethanolamine (TEA)-based esterquat cationic surfactant using an artificial neural network," *Molecules*, vol. 16, pp. 5538–5549, 2011.

Hindawi Publishing Corporation
Journal of Chemistry
Volume 2013, Article ID 158431, 10 pages
http://dx.doi.org/10.1155/2013/158431

Research Article

Self-Organization-Based Fabrication of Stable Noble-Metal Nanostructures on Large-Area Dielectric Substrates

Victor Ovchinnikov[1] and Andriy Shevchenko[2]

[1] *School of Electrical Engineering, Aalto Nanofab, Aalto University, P.O. Box 13500, 00076 Aalto, Finland*
[2] *Department of Applied Physics, School of Science, Aalto University, P.O. Box 13500, 00076 Aalto, Finland*

Correspondence should be addressed to Victor Ovchinnikov; victor.ovchinnikov@aalto.fi

Received 15 January 2013; Accepted 28 February 2013

Academic Editor: Pietro Calandra

A cost-effective fabrication of random noble-metal nanostructures with a feature size of the order of 10 nm on a large-area dielectric substrate is described. The method combines dry etching of the substrate through a self-organized metal mask with a directional deposition of a multilayered metal film. The technique allows one to create metal nanoislands on a nanopatterned dielectric template with an enhanced adhesion between the metal and the dielectric. The use of the adhesion layer—that makes the structures stable—is important in view of variety of optical and other potential applications of the structures. We observe that the presence of the adhesion sublayer dramatically influences both the morphological and optical properties of the structures. The results of this work can be of interest in regard to the development of new approaches to self-organization-based nanofabrication of extremely small metal and metal-dielectric nanostructures on large-area substrates.

1. Introduction

Metal nanostructures have widespread applications in many areas of science and technology, such as chemical and biological sensing [1], subwavelength imaging [2], and plasmonic nanomaterials [3]. The majority of these applications rely on optical excitation of plasmon resonances in metal nanoparticles that can be either isolated or arranged in a nanoparticle array. Spectral properties of these resonances can be adjusted by tailoring the size, shape, and separation distance of the nanoparticles. The well-studied *periodic* nanopatricle arrays, which, in particular, are very attractive from a theoretical point of view, are difficult to fabricate on large-area substrates and, therefore, their mass production is a challenging task. Traditional semiconductor technology offers reliable and reproducible process flows, but their acceptance as a general fabrication tool for obtaining large-area metal nanostructures has been hindered by two drawbacks: (1) a limited resolution of optical lithography and (2) a lack of efficient dry etching techniques for most metals. Because of this, a dominant fabrication method for obtaining regular metal nanostructures is electron beam lithography (EBL) with lift-off removal of useless metal. However, by using this technique, it is difficult to obtain features smaller than 50 nm. In addition, the fabrication approach based on EBL requires a rather long processing time, which makes it not only time-consuming, but also expensive to fabricate large-area arrays of nanostructures.

As alternatives to step-by-step patterning by conventional EBL, several nonlithographic methods—for example, based on self-organization phenomenon—have been demonstrated to produce nanostructures in parallel way. These techniques allow large-area substrates to be nanostructured using fast and low-cost fabrication steps. The functional properties of the nanostructures, however, are less controllable due to the inherent randomness in the size, shape, and spacing of the created particles. In spite of this, random nanostructure arrays are widely used, for example, as catalysts in fabrication of carbon nanotubes [4], light trapping layers in thin-film solar cells [5, 6], magnetic nanodot arrays [7], SERS substrates [8], and environment sensors [9]. Examples of fast and cost-effective nonlithographic techniques are nanosphere lithography [10], nanofabrication using porous alumina templates [11] and so-called oblique angle deposition [12].

One of the fastest and most cost-effective nanofabrication approaches is an approach making use of self-assembly of metal nanostructures on a surface with poor adhesion, for example, Au or Ag nanoislands on glass [13, 14]. This method possesses high resolution and, what is practically important, full compatibility with standard semiconductor fabrication technology. By the nature of the phenomenon, self-organization takes place in a thin layer of noble metal on a dielectric substrate at nonequilibrium thermodynamic conditions, when the adhesion of the metal to the substrate is weak. Such self-organized nanoparticle arrays are *not* mechanically stable and can easily be damaged—for example, rinsing the sample in water can completely destroy the array. Hence, such arrays are nearly impossible to incorporate in more complicated, multilayered devices.

In this work, a self-organization-based approach to nanofabrication of large-area arrays of metal nanostructures on a dielectric substrate with an adhesion sublayer is demonstrated. This is done by creating identical lace-like Au and Ag nanostructures with and without Ti sublayer on glass and oxidized silicon substrates. In particular, these nanostructures allow us to directly study the influence of the adhesion layer on the morphology and optical properties of the samples. We note that noble metal nanostructures *without* an adhesion sublayer cannot be created by using a lift-off-based fabrication method, such as EBL, and, consequently, direct estimation of the influence of such a layer on the optical properties of the sample is impossible; some experimental studies of the influence of the adhesion-layer *thickness* on the properties of a *flat* metal film can be found in [15–17].

In the following section, we introduce our fabrication method and describe in detail the sample preparation and measurement procedures. The next section consists of two subsections. In the first one, the morphology of the fabricated nanostructures is studied on the basis of SEM images of the samples obtained at different deposition conditions. The second subsection describes the transmittance, reflectance, absorptance, and SERS spectra of these samples. The last section summarizes our results.

2. Materials and Methods

2.1. Fabrication Method. Our fabrication method is based on (i) self-assembly of metal nanostructures on a dielectric substrate, (ii) fabrication of a nanostructured template by etching the substrate through the self-organized metal mask, and (iii) directional deposition of several different metal layers on the obtained template. In principle, for the template preparation, any nanopatterning method that provides vertical sidewalls can be used (e.g., etching through lithographically fabricated masks or self-organized structures and even direct writing by a focused laser or ion beam [18, 19]).

We start by creating a self-organized gold or silver nanostructures which are then used as a mask for anisotropic dry etching of the substrate (Figure 1(a)). To create the mask, a thin layer of gold or silver is evaporated onto an oxidized silicon or glass substrate at a low deposition rate. If the layer thickness does not exceed 15 nm, the film made of gold shows a lace-like structure owing to the poor adhesion of the metal to silicon oxide. An additional annealing after the deposition can be employed to modify the mask morphology. In contrast to gold, silver tends to form spheroidal nanoislands with the average size and separation controlled by the deposition and annealing parameters [6].

The poor adhesion of gold and silver to the dielectrics limits the etching methods for the substrate patterning. Wet etching cannot be used, because of destructive surface-tension forces and diffusion of the liquid etchant beneath the metal. Dry etching, on the other hand, can be successfully used. In addition, dry etching, such as reactive ion etching (RIE), provides vertical sidewalls for the nanostructures. Therefore we use RIE for etching the dielectric through the obtained mask (Figure 1(b)).

In the next step, the residues of the metal mask are removed by selective wet etching to obtain a template that is made of the substrate material only (see Figure 1(c)). The template elements perfectly replicate the geometry of the mask. Then the template is covered with a thin adhesion layer of an easily oxidized metal (such as Ti or Cr). At atmospheric ambient conditions, the adhesion layer that is not protected by any other material layer is readily oxidized and does not affect much the functional properties of the nanostructures. It is important to deposit the adhesion layer only on the flat (horizontal) surfaces of the template and leave the sidewalls uncovered (Figures 1(d)–1(f)). This helps one to avoid unwanted deposition of the next metal layer onto the sidewalls and, thus, to better preserve the desired nanostructure geometry. This requirement is fulfilled by using a directional flux of deposited material, for example, e-beam evaporation at normal incidence. Even if some noble-metal particles turn out to be deposited onto the sidewalls, they can easily be removed, owing to their poor adhesion, by rinsing the sample in an ultrasonic bath.

The final step is to coat the template with a functional metal layer—with a gold or silver layer in our case. This should be done immediately after the deposition of the adhesion layer in order to prevent possible oxidation of the latter. This metal coating can be done in two different ways. In the first one, the metal is evaporated onto the wafer surface at normal incidence. Therefore, a metal layer is formed simultaneously on the elevated surfaces of the nanostructure and at the bottom of the template (Figure 1(d)). The second way is to evaporate the metal onto the template at an angle. The sample can be either rotated (Figure 1(f)) or kept still during the deposition (Figure 1(e)). The rotation provides a uniform covering of the structure upper parts, while the static deposition leads to formation of asymmetric nanostructures that, for example, can exhibit optical anisotropy [20]. The extent to which the sidewalls are covered with metal depends significantly on the evaporation angle α counted from the normal of the substrate surface (Figure 1(e)) [21].

2.1.1. Experimental Details. The samples were fabricated either on borosilicate glass plates or on oxidized silicon substrates with (100)-orientation. The sample size is $22 \times 22 \times 0.5\,\text{mm}^3$. The substrate cleaning procedure starts with

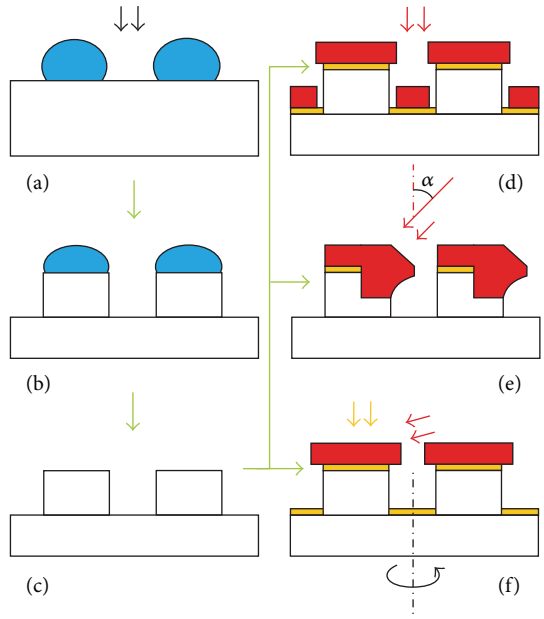

FIGURE 1: Schematic of the process of self-organization-based nanofabrication of stable noble-metal nanostructures on a dielectric substrate. The process consists of four steps. The fourth step is chosen to correspond to either (d), (e), or (f).

sonification of the sample in acetone and 2-propanol. Then the sample is RCA-1 cleaned for 10 minutes and processed in oxygen plasma during 1 minute. This pretreatment is needed to equalize the surface conditions over the whole substrate. The Si samples with a 60 nm thick layer of SiO_2 were used to optimize the whole fabrication process, since they make it possible to observe the fabricated nanostructures with SEM. We note that all the process steps lead to identical results on glass and on silicon oxide.

The metal films were deposited with the help of an e-beam evaporation system IM-9912 (Instrumentti Mattila Oy) with adjustable substrate inclination and rotation speed at the base pressure of 4×10^{-7} Torr at room temperature. The deposition rate for each film was measured by using quartz crystal microbalance.

The RIE of the templates was done in a 13.56 MHz driven parallel electrode reactor Plasmalab 80 Plus (Oxford Instruments Plasma Technology). An anisotropic etching process based on fluorine chemistry (gas mixture $CF_4 : CHF_3 = 1:3$) was used for the glass and SiO_2 etching. The etching experiments were performed at a total gas flow of 80 sccm, pressure of 30 mTorr and rf power of 40 W. The remaining gold was removed in aqua regia (1 : 3 volume mixture of 69% HNO_3 and 37% HCl, resp.) during 20 s at room temperature, resulting in lace-like structures in SiO_2 or glass. Mask annealing was done at 400 C during 20 min in N_2 ambient.

SEM images of the fabricated samples were taken with Zeiss Supra 40 field emission scanning electron microscope. The transmittance and reflectance spectra of the samples were measured at normal incidence by using PerkinElmer Lambda 950 UV-VIS spectrometer in the spectral range from 300 to 850 nm. The reflectance spectra were measured by collecting the directly reflected and backscattered light with an integrating-sphere detector. The surface enhanced Raman scattering (SERS) of the molecules of methylene blue (MB) on the fabricated substrates was studied by using a WITec Alpha 300 Raman microscope equipped with a frequency-doubled Nd:YAG laser (532 nm) as the excitation source. A water solution of methylene blue at a concentration of 3×10^{-4} M was used as a test analyte.

3. Results and Discussion

3.1. SEM Observations. To demonstrate the performance of the method described in Section 2, we have fabricated gold and silver lace-like nanostructures. In order to study the effect of an adhesion layer beneath the metal, some of the samples were fabricated by directly metal-coating the patterned SiO_2 or glass surface and some other samples included an additional adhesion sublayer of Ti. Such mechanically stable noble-metal nanostructures are of interest in view of variety of nanooptical applications. Figures 2–7 illustrate the most essential steps of practical realization of the method depicted in Figure 1. As an etching mask (Figure 1(a)), we use the nanostructures formed on a dielectric surface during the physical vapor deposition of gold or silver, although other metals with poor adhesion to the substrate could also be used.

The shape and size of the lace-like Au nanostructures can be controlled by varying the fabrication parameters and conditions at each step of the process. It is important to notice that the main features of the nanopattern to be fabricated are defined already at the initial metal deposition stage. Figures 2 and 3 show self-organized metal nanostructures produced by coating an oxidized silicon surface with gold and silver, respectively, using the e-beam evaporation. SEM images of the samples with four different thicknesses of the coating were taken. The metals are observed to produce a variety of the nanostructure geometries with different size distributions. For both metals, the thicker the deposited layer, the larger the fraction of the metal-covered area and the sizes of the eventually obtained nanofeatures. The difference between the patterns made of gold and silver is significant. In the case of gold, continuous net- or lace-like structures with narrow channels are observed, while when using silver, well-separated nanoparticles of various shapes and sizes appear to cover the whole surface of the substrate. The geometry of such metal masks depends on many factors, such as surface diffusion characteristics, the flux of the deposited material, and the concentration of the nucleation centers on the surface. In this context, the film thickness is the most essential adjustable parameter that can be used to control the structure geometry. For example, a 15 nm thick gold film shown in Figure 2(d) exhibits smaller widths and a lower density of the empty channels than a 10 nm thick film deposited at the same deposition conditions (see Figure 2(b)). A 4 nm thick silver film (Figure 3(a)), on the other hand, shows approximately six times higher density of the nanoislands than a 12 nm thick film (Figure 3(d)). The maximum obtainable average size of the nanoislands is limited by their coalescence and transformation into a continuous film. When dealing with gold and

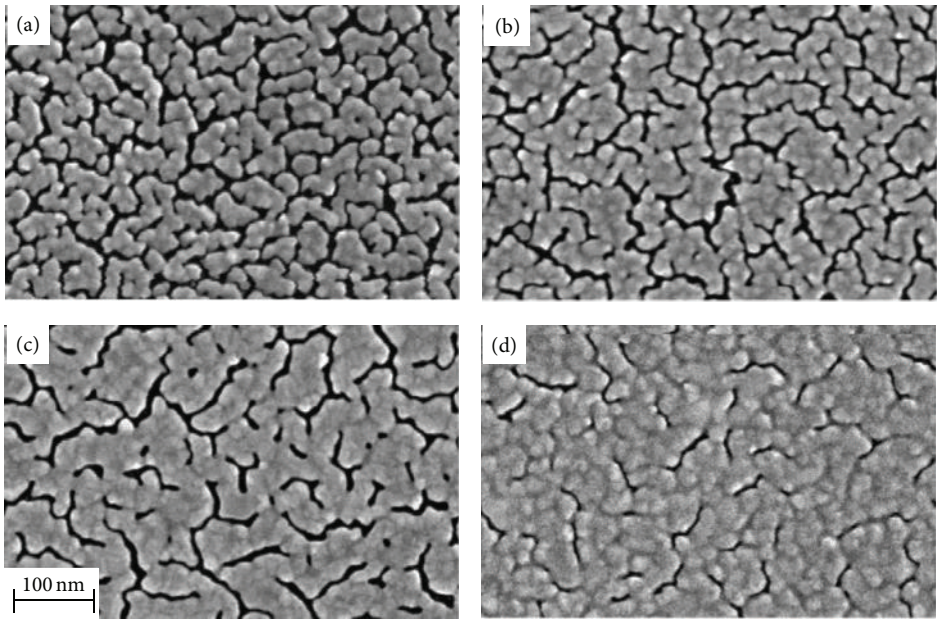

Figure 2: SEM images of Au films directly deposited on a flat dielectric substrate. The film thickness is 8, 10, 11, and 15 nm in (a), (b), (c), and (d), respectively.

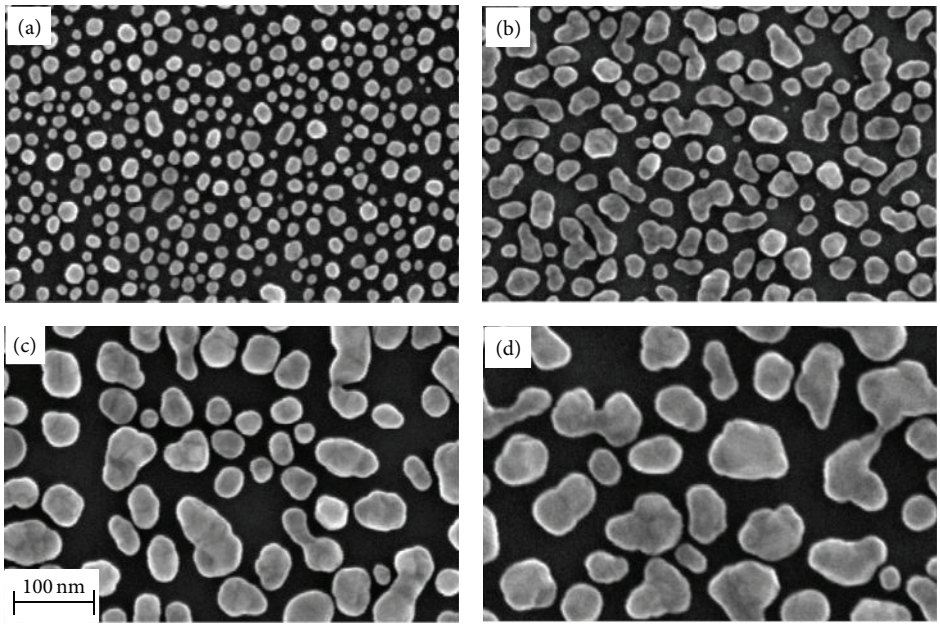

Figure 3: SEM images of Ag films directly deposited on a dielectric substrate. The film thickness is 4, 5.5, 10, and 12 nm in (a), (b), (c), and (d), respectively.

silver, this transformation takes place if the film thickness exceeds 20 nm. An additional control of the mask pattern geometry can be provided by changing the metal deposition rate, substrate temperature, and surface properties.

Compared to well-known self-organized Au and Ag masks [22], the masks created in the present study do not require any annealing. The directly deposited self-organized films are used in their original form, which allows keeping the feature sizes small. On the other hand, annealing is an excellent tool for further shaping and sizing of the created metal pattern. Due to combined effects of a weak adhesion force, increased surface diffusion, and thermal stresses, the structures can be fully rearranged during the annealing. Figure 4 provides a direct comparison of the pattern

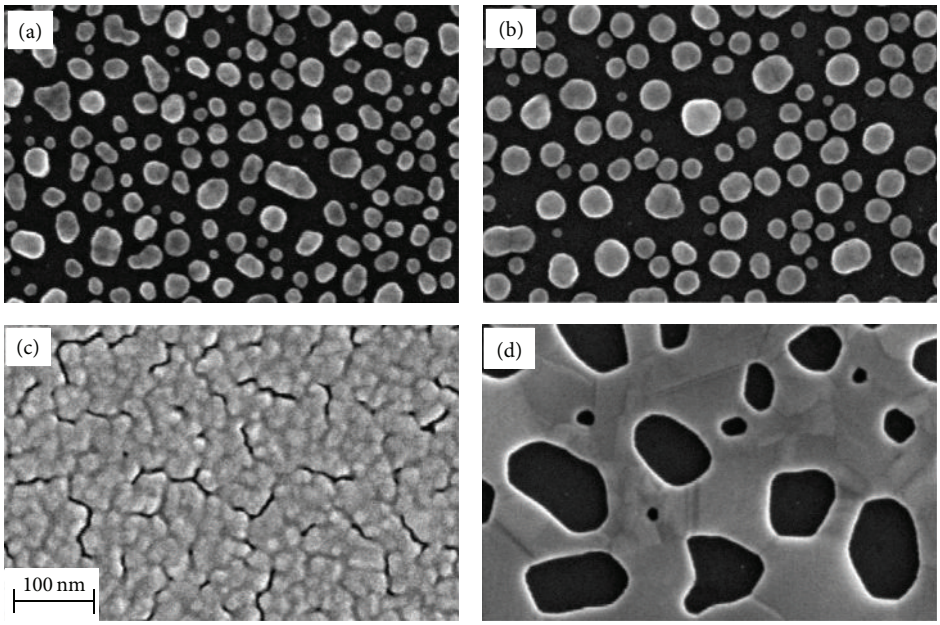

Figure 4: SEM images of thin layers of Ag (cases (a) and (b)) and Au ((c) and (d)) before ((a) and (c)) and after ((b) and (d)) annealing at 400°C. The thicknesses of Ag and Au layers are 5 and 15 nm, respectively.

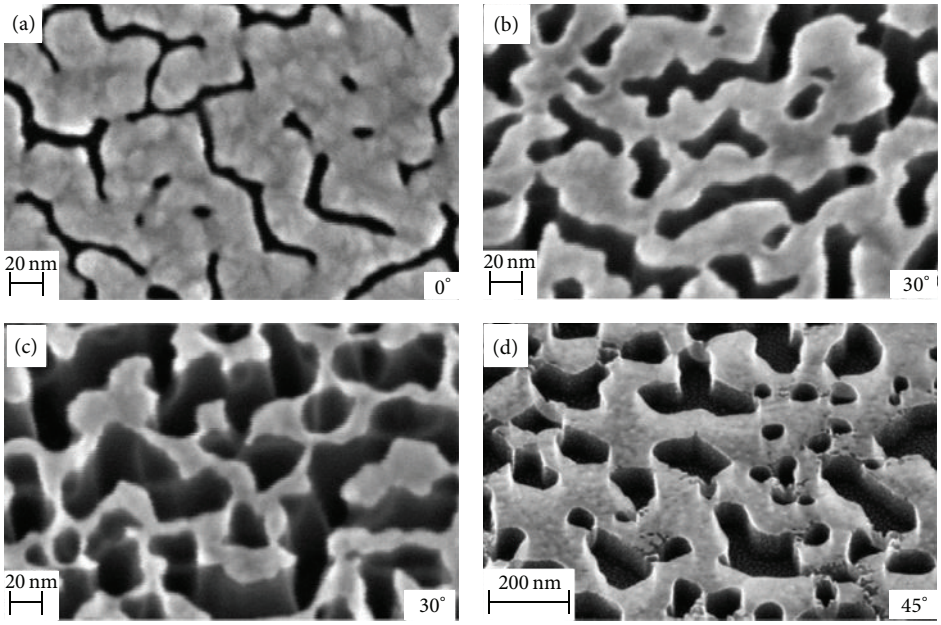

Figure 5: SEM images of nanstructures produced by RIE: (a) Au mask, (b) and (c) the samples after etching the substrate during 20 and 25 min, respecticely, and (d) a sample of Figure 4(d) with extra nanoholes appeared in the mask. The view angles are shown.

geometry before and after annealing of silver and gold films. In the case of silver (see Figures 4(a) and 4(b)), the annealing results in larger and more round nanoislands with a narrower size distribution. In contrast, annealing of a lace-like pattern in gold makes the narrow channels in the pattern disappear, and we obtain a smooth metal film with large irregular holes (see Figures 4(c) and 4(d)).

While arrays of metal nanospheroids and nanoholes in a thin metal film have been previously extensively studied, the nanostructures of gold and silver with the geometry and

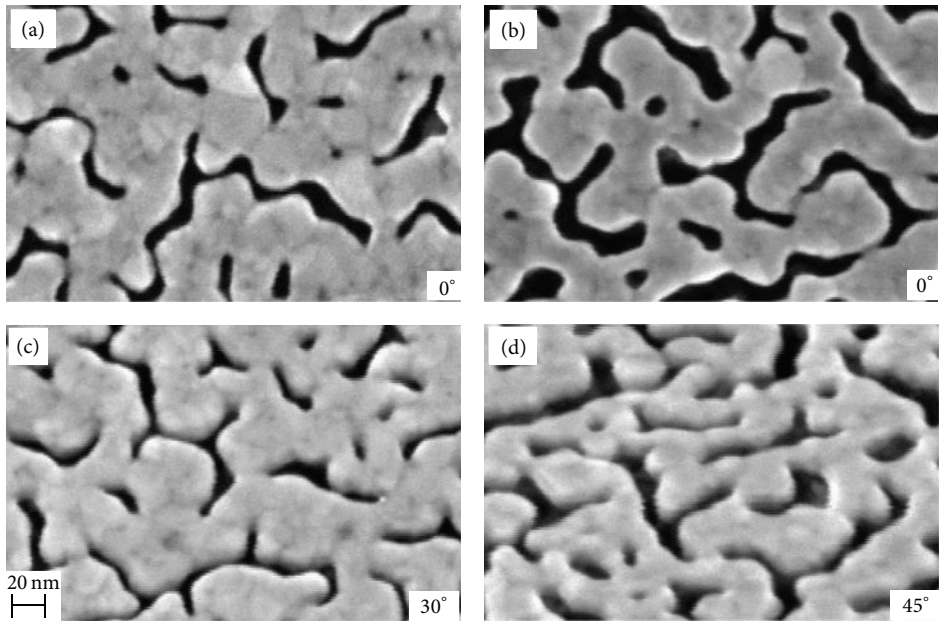

Figure 6: Plain and tilted SEM images of 16 nm thick Au nanostructures with a 1 nm thick sublayer of Ti: the structures (a) and (c) are created on the template of Figure 5(b) and the structures (b) and (d) on the template of Figure 5(c). Here $\alpha = 0$. The view angles are presented.

dimensions of the patterns as in Figure 2 were not studied much. Hence, our further investigations are focused on the creation and optical characterization of this type of metal nanostructures.

The lace-like pattern of Figure 2(a) is inherent to gold. In the following, we describe a technique that can be used to fabricate such structures out of any metal. We start by creating an elevated nanostructure array (similar to a nanopillar array) by means of dry etching through the prepared gold mask (see Figure 1(b)). This mask, obtained by deposition of an 8 nm thick layer of gold at a rate of 1.0 Å/s, contains depressions (in the form of narrow channels) and protrusions (see Figures 2(a) and 5(a)). The average width of the channels is ca. 7 nm, and the width of the protrusions is about 30 nm. The mask thickness is a critical parameter for performing RIE, because it determines the maximum obtainable etching depth. Up to a certain etching depth (say, up to 60 nm), the mask pattern remains essentially unchanged (see Figure 5(b)) and the widths of the channels transferred to SiO_2 are nearly equal to those in the mask. However, further etching results in widening of the channels, which can start to destroy the original mask pattern by deforming the protrusion tops (Figure 5(c)). This is caused by erosion of the gold mask during the ion bombardment. Note that the maximum sputtering yield is reached at a nonzero sputtering angle, that is, not for a normal direction of the sputtering. As a consequence, any deviation of the original mask sidewalls from vertical leads to developing a wedge of etching (an inclined mask sidewall) which, in turn, causes the mask size shrinking. The maximum etching depth of 75 nm was reached in 25 min of RIE (Figure 5(c)), which resulted in an increase of the channel width to about 25 nm.

We have also used an annealed film of Figure 4(d) as an etching mask and obtained vertical, 80 nm high sidewalls after a 15 min processing by RIE (see Figure 5(d)). The difference of the RIE result is explained by the difference of the mask structure. Since the holes have vertical gold sidewalls, they are not subjected to the generation of the etching wedge. On the other hand, the lace-like structures have somewhat curved sidewalls, which facilitates the appearance of the fast etched planes. The etching through the hole structure exhibits one more feature. The thickness of the mask is never completely uniform, which in the SEM images is seen as darker and lighter spots distributed over the mask. In the dark spots, the metal is thinner, which can lead to appearance of additional small nanoholes in the mask during the etching procedure (see Figure 5(d)).

The etching results in elevated SiO_2 nanostructures with gold residues on the top. These structures can exhibit localized surface plasmon resonances that can be used for optical applications. However, the presence of surface damages caused by RIE can destructively affect the plasmonic properties of the structures. In addition, the sizes and shapes of the metal residues are difficult to control. Therefore, we remove the metal residues from the obtained template—by selective wet etching—and obtain a pure nanostructured template in SiO_2/Si or glass (Figure 1(c)) that closely repeats the lateral geometry of the etching mask.

In the next step, the obtained template is used as a substrate for deposition of an arbitrary metal with or without an adhesion sublayer. As shown in Figure 1(d), the adhesion layer (Ti) is deposited at normal incidence (the substrate tilt angle α is equal to 0°). A functional layer of Au or Ag is then deposited at an angle α of either 0° (see Figure 1(d))

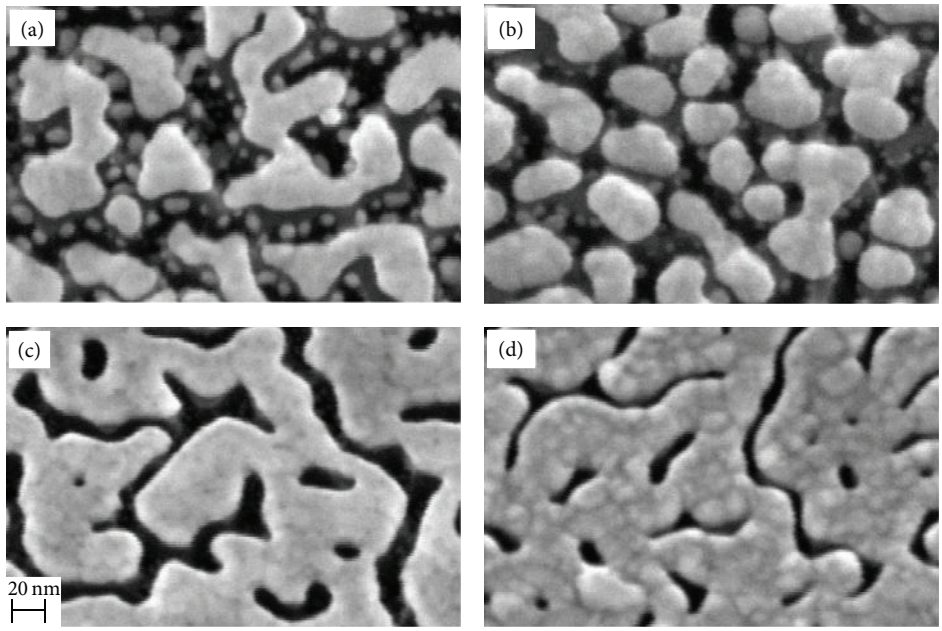

Figure 7: SEM images of an 8 nm thick nanostructures made of Au (cases (a) and (c)), and Ag ((b) and (d)) without ((a) and (b)), and with ((c) and (d)) a sublayer of Ti. In (a) and (c), $\alpha = 0$. In (b) and (d), $\alpha = 70^{\circ}$; the samples were rotated during the deposition. The view angle is 30°.

or 70°. In the later case, the substrate can stay motionless (Figure 1(e)) to form asymmetric nanostructures or to be rotated to obtain a uniform metal coating of the template's *upper* surface (Figure 1(f)). Figures 6(a) and 6(b) illustrate the results of deposition a gold films of the same thickness onto the templates of Figures 5(b) and 5(c), respectively, at normal incidence. Figures 6(c) and 6(d) show tilted views of these samples. It can be seen that evaporation of 1 nm thick layer of Ti and subsequent evaporation of 16 nm thick layer of Au onto the templates leads to a reduction of the average width of the channels (from 16 to 7 nm and from 25 to 11 nm for templates of Figures 5(b) and 5(c), resp.). This result is not obvious, because the deposited gold atoms arrive at the template moving along the normal to the substrate surface. To obtain some information on the mechanism of the nanostructure metallization, we consider a tilted view of the same sample (Figures 6(c) and 6(d)). The sharp contours of the template protrusions are seen to be covered with smoothly curved edges of the deposited gold layer hanging down over the channel edges. Thus, the vertical growth of the gold film is accompanied by a lateral one, despite the unidirectional deposition of the atoms. Presumably, this originates from surface diffusion of atoms that, during the deposition, receive an excess kinetic energy on the surface. If an adhesion layer is not used, the deposited metal tends to form nanospheroids on the top and sidewalls of the template protrusions.

The influence of a Ti sublayer on the nanostructure morphology was studied further by fabricating two more samples, in which an 8 nm thick layer of either Au or Ag on Ti is deposited at normal incidence onto the template of Figure 5(c). The pure gold nanostructures (shown in Figure 7(a)) do not exactly follow the template pattern geometry, in contrast to the Ti/Au structures shown in Figure 7(c). Instead, they are broken into shorter segments and surrounded by many small nanoclusters. This implies that, on the top surfaces of the template protrusions, gold tends to migrate toward the centers of the isolated areas. On the other hand, the protrusion sidewalls are also favorable places for gold cluster nucleation, but due to a limited amount of the arrived gold, these clusters are very small in size. In the case of deposition of Au onto Ti (Figure 7(c)), the surface diffusion of the gold atoms is significantly reduced and, as a result, the film grows uniformly. The growth rate of the film is slightly higher at the edges of the protrusions than on the top, which leads to formation of a rim at the edges. This rim shadows the sidewalls and partly the bottom surfaces of the channels from coating by the metal. Simultaneously it reduces the channel widths. The lateral growth rate of the rim can be increased by tilting and rotating the substrate during the deposition.

Figures 7(b) and 7(d) show the lace-like Ag and Ti/Ag structures, in which an 8 nm thick film of silver is formed at a deposition angle of 70° on a rotating template. The templates were identical for these two films and they were similar to the one shown in Figure 5(b). The substrate tilting and rotation result in more reduced average width of the channels in the Ti/Ag film (Figure 7(d)) compared to what was obtained in the Ti/Au film (Figure 7(c)). We remind that the latter film was deposited at normal incidence. Silver islands on the template without Ti (Figure 7(b)) are seen to have more

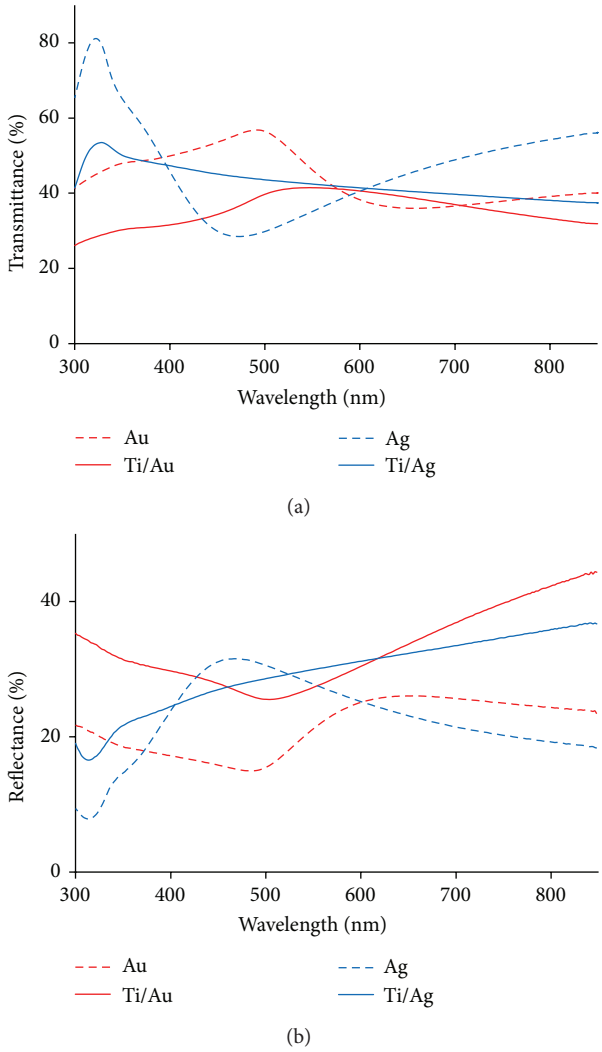

FIGURE 8: Transmittance (a) and reflectance (b) spectra of 8 nm thick Au nanostructures with and without Ti on glass. The metal is deposited at $\alpha = 70^{\circ}$ (the samples were rotated during the deposition).

rounded edges and a narrower size distribution than the gold islands (Figure 7(a)). The samples with Ti as before accurately repeat the template geometry.

3.2. Optical Properties of Lace-Like Metal Nanostructures. The novel lace-like gold and silver nanostructures described in the above section are of interest in view of optical applications, in particular in optical spectroscopy, since they are likely to exhibit surface plasmon resonances (SPRs). To prepare a template suitable for spectroscopic analysis of the structures, we have etched an *optically transparent* glass substrate through a self-assembled gold mask, during 16 min in the RIE reactor. The etching resulted in the creation of 65 nm deep channels in the substrate. Then, we coated some of the substrates with an adhesion layer of Ti and deposited an 8 nm thick layer of the metal of interest (gold or silver) at different tilt angles of the substrate. The geometries of the structures are similar to those illustrated in Figure 7. In order to compare the optical properties of these samples with those of metal films on a flat substrate, we have also coated the reference glass samples with 8 nm thick films of gold and silver. The reference sample made of gold (silver) has a quite similar lace-like (spherical-island) geometry as the samples obtained on the etched substrates without Ti.

The optical transmittance and reflectance spectra of the fabricated gold and silver nanostructures are shown in Figure 8. The randomness in the island sizes and shapes and a strong interaction between the islands lead to spectral broadening of the overall plasmonic response of the sample [20, 23]. The gold samples without a Ti sublayer (red dashed curves) show spectral features that refer to a Fano-type resonance [24] at the wavelengths from about 500 to 600 nm, presumably resulting from an interplay between narrowband plasmon resonances at the edges of the structures and broadband lateral SPR excitations in the islands at longer wavelengths. We note that even though the resonance is not very sharp, the sample can still be expected to provide a high local enhancement of the incident field at the positions of the nanoisland edges. The spectra of the nanostructures with a Ti adhesion layer (solid curves) differ quite significantly from those of the structures without Ti. A red shift and broadening of the maximum transmittance band can be explained by the influence of Ti that is known to increase both the real and imaginary parts of the effective refractive index and suppress plasmonic resonant excitations.

Similarly to the spectra of the samples with gold, the spectra of silver lace-like structures fabricated without a Ti sublayer exhibit pronounced resonant features. A broad and relatively strong Fano-type resonance is now observed at shorter wavelengths, between ca. 300 and 500 nm. It is remarkable, however, that introduction of a 2 nm thick Ti layer beneath silver nearly completely flattens the spectrum, and only weak sings of short-wavelength SPRs, between 300 and 350 nm, can still be observed in the spectra. Thus, a sublayer of Ti dramatically suppresses SPRs, especially at longer wavelengths.

To receive more information about the SPR excitations and spectral modifications by the Ti sublayer, we have evaluated also the absorptance spectra. This was done by using the equation $A = 1 - T - R$, where A, T, and R are absorptance, transmittance, and reflectance, respectively. The results of these calculations are shown in Figures 9(a) and 9(b) for gold and silver nanostructures, respectively. A crucial difference can be observed between the absorptance spectra of the fabricated structures with and without the titanium sublayer (see the dashed and solid curves). For both Au and Ag samples, the presence of Ti leads to a decreased absorptance in the blue and an increased absorptance in the red and near-infrared spectral range. The main reason of this difference is in our opinion a significant suppression of the SPRs.

Local enhancement of optical fields by metal nanostructures cannot always be observed in the far-field transmittance and reflectance spectra. Thus, in order to reveal a possible near-filed enhancement by our lace-like nanostructures, we have used them as SERS substrates. A Raman spectrum of MB

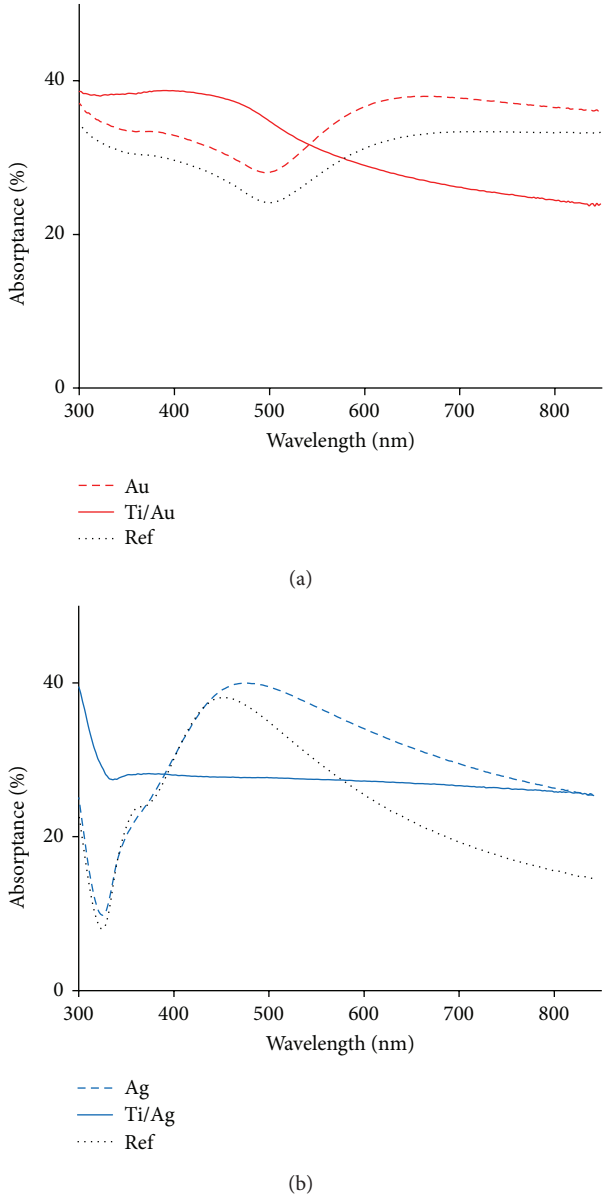

FIGURE 9: Effect of 2 nm thick layer of Ti on the absorptance of 8 nm thick nanostructures made of Au (a) and Ag (b) on glass. The deposition angle is $\alpha = 70^{\circ}$. The samples were rotated during the deposition. "Ref" stands for an 8 nm layer of gold on glass, without Ti.

molecules adsorbed directly on an oxidized silicon substrate is shown by the black curve in Figure 10 (the peak at 530 cm^{-1} wavenumber is due to Raman scattering by crystalline Si). This spectrum is used as a reference. The sample obtained by coating a nanopatterned *glass* template with a Ti/Ag layer (2 nm of Ti and 8 nm of Au) shows an order of magnitude enhancement of the SERS signal (see the blue curve; the spectrum can be compared with the one reported in [25]). Thus, in spite of the smallness of our nanostructures and a significant suppression of SPRs by Ti, our structures provide a clear local enhancement of the optical near-field. It is interesting that the Raman signal can be even further enhanced

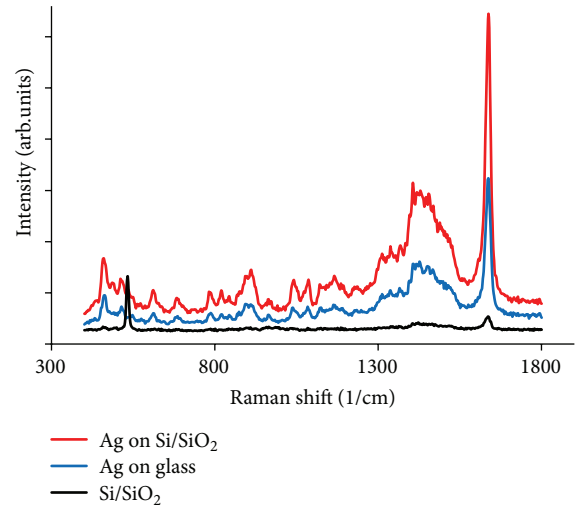

FIGURE 10: SERS spectra of MB adsorbed on an 8 nm thick Ag nanostructures on an oxidized Si wafer (red curve; the oxide thickness is 60 nm) and on glass (blue curve). A 2 nm thick adhesion layer of Ti was used in both samples. The deposition was done at $\alpha = 70^{\circ}$ with rotation. The black curve is the spectrum of MB on Si/SiO_2.

by using an oxidized Si as a template material instead of glass. The red curve in Figure 10 shows a SERS spectrum of MB measured on such a nanostructured $Si/SiO_2/Ti/Ag$ sample. The additional enhancement can have the origin in the fact that the interface between Si and SiO_2 reflects a part of the transmitted light back to the nanostructures. This reflected optical field makes an additional contribution to the Raman signal [26].

4. Conclusions

We have proposed and demonstrated a technique for fabrication of random metal nanostructures with the characteristic size on the order of 10 nm on a large-area dielectric substrate. The technique is based on self-organization of metal nanoislands with poor adhesion to the substrate. These islands are used as a mask for etching the substrate material. Afterwards, the etched substrate is directionally coated with any metal of interest to create similar nanoislands out of this metal. Using this technique, it is easy to fabricate the samples *with and without* an adhesion layer between the metal and the substrate. The adhesion layer makes the nanostructures mechanically stable and, therefore, they can be integrated in a more complicated device or used as plasmonic sensors for liquid or even solid analytes.

We have measured optical spectra of the fabricated lace-like nanostructures made of gold and silver and studied the influence of Ti sublayer on their properties. The presence of a very thin adhesion layer (e.g., of 2 nm thickness) was observed to significantly suppress the SPR excitations in the structures, and, in addition, to increase optical absorption. In spite of this, the fabricated Ti/Ag nanostructures considerably enhanced the Raman transitions of methylene blue, which

refers to a considerable local enhancement of the light intensity by the structures. The described fabrication technique can be optimized and further developed towards specific applications in science and technology, for example, in optical sensing and surface enhanced scattering and absorption spectroscopy.

Acknowledgments

The authors acknowledge the financial support from the Academy of Finland (Project no134029). This research was undertaken at the Micronova Nanofabrication Centre, supported by Aalto University.

References

[1] J. N. Anker, W. P. Hall, O. Lyandres, N. C. Shah, J. Zhao, and R. P. Van Duyne, "Biosensing with plasmonic nanosensors," *Nature Materials*, vol. 7, pp. 442–453, 2008.

[2] X. Zhang and Z. Liu, "Superlenses to overcome the diffraction limit," *Nature Materials*, vol. 7, pp. 435–441, 2008.

[3] E. Cortes, L. Mochán, B. S. Mendoza, and G. P. Ortiz, "Optical properties of nanostructured metamaterials," *Physica Status Solidi B*, vol. 247, pp. 2102–2107, 2010.

[4] Y. F. Guan, A. V. Melechko, A. J. Pedraza, M. L. Simpson, and P. D. Rack, "Non-lithographic organization of nickel catalyst for carbon nanofiber synthesis on laser-induced periodic surface structures," *Nanotechnology*, vol. 18, no. 33, Article ID 335306, 2007.

[5] X. Sheng, J. Liu, I. Kozinsky et al., "Design and non-lithographic fabrication of light trapping structures for thin film silicon solar cells," *Advanced Materials*, vol. 23, pp. 843–8847, 2011.

[6] C. Eminian, F. J. Haug, O. Cubero, X. Niquille, and C. Ballif, "Photocurrent enhancement in thin film amorphous silicon solar cells with silver nanoparticles," *Progress in Photovoltaics*, vol. 19, no. 3, pp. 260–265, 2011.

[7] M. T. Rahman, N. N. Shams, and C. H. Lai, "Nonlithographic fabrication of 25 nm magnetic nanodot arrays with perpendicular anisotropy over a large area," *Journal of Applied Physics*, vol. 105, no. 7, Article ID 07C112, 2009.

[8] M. Fan, G. F. S. Andrade, and A. G. Brolo, "A review on the fabrication of substrates for surface enhanced Raman spectroscopy and their applications in analytical chemistry," *Analytica Chimica Acta*, vol. 693, no. 1-2, pp. 7–25, 2011.

[9] E. Galopin, A. Noual, J. Niedziółka-Jönsson, M. Jönsson-Niedziółka et al., "Short- and long-range sensing using plasmonic nanostructures: experimental and theoretical studies," *Journal of Physical Chemistry C*, vol. 113, pp. 15921–15927, 2009.

[10] X. Zhang, L. Zhang, M. Gao, W. Zhou, and S. Xie, "High-resolution nanosphere lithography (NSL) to fabricate highly-ordered ZnO nanorod arrays," *Journal of Nanoscience and Nanotechnology*, vol. 10, no. 11, pp. 7432–7435, 2010.

[11] Y. Piao and H. Kim, "Fabrication of nanostructured materials using porous alumina template and their applications for sensing and electrocatalysis," *Journal of Nanoscience and Nanotechnology*, vol. 9, no. 4, pp. 2215–2233, 2009.

[12] S. Jayawardhana, G. Kostovski, A. P. Mazzolini, and P. R. Stoddart, "Optical fiber sensor based on oblique angle deposition," *Applied Optics*, vol. 50, no. 2, pp. 155–162, 2011.

[13] J. Sancho-Parramon, V. Janicki, M. Lončarić, H. Zorc, and P. Dubček, "Optical and structural properties of Au-Ag islands films for plasmonic applications," *Applied Physics A*, vol. 103, no. 3, pp. 745–748, 2011.

[14] V. Ovchinnikov and A. Priimagi, "Anisotropic plasmon resonance of surface metallic nanostructures prepared by ion beam mixing," in *Proceedings of the 1st International Conference on Quantum, Nano, and Micro Technologies (ICQNM '07)*, Guadaloupe, Mexico, January 2007.

[15] B. Lahiri, R. Dylewicz, R. M. De La Rue, and N. P. Johnson, "Impact of titanium adhesion layers on the response of arrays of metallic split-ring resonators (SRRs)," *Optics Express*, vol. 18, no. 11, pp. 11202–11208, 2010.

[16] K. W. Vogt, P. A. Kohl, W. B. Carter, R. A. Bell, and L. A. Bottomley, "Characterization of thin titanium oxide adhesion layers on gold: resistivity, morphology, and composition," *Surface Science*, vol. 301, no. 1–3, pp. 203–213, 1994.

[17] H. Aouani, J. Wenger, D. Gérard et al. et al., "Crucial role of the adhesion layer on the plasmonic fluorescence enhancement," *ACS Nano*, vol. 3, no. 7, pp. 2043–2048, 2009.

[18] K. C. Vishnubhatla, S. Venugopal Rao, R. Sai Santosh Kumar, R. Osellame, S. N. B. Bhaktha, S. Turrell et al., "Femtosecond laser direct writing of gratings and waveguides in high quantum efficiency erbium-doped Baccarat glass," *Journal of Physics D*, vol. 42, Article ID 205106, 2009.

[19] R. M. Langford, "Focused ion beam nanofabrication: a comparison with conventional processing techniques," *Journal of Nanoscience and Nanotechnology*, vol. 6, pp. 661–6668, 2006.

[20] A. Shevchenko and V. Ovchinnikov, "Magnetic excitations in silver nanocrescents at visible and ultraviolet frequencies," *Plasmonics*, vol. 4, no. 2, pp. 121–126, 2009.

[21] V. Ovchinnikov and A. Shevchenko, "Large-area arrays of pillar-based metal nanostructures," in *Proceedings of the 3rd International Conference on Quantum, Nano and Micro Technologies (ICQNM '09)*, pp. 125–129, Cancún, Mexico, February 2009.

[22] G. Gupta, Y. Nakayama, K. Furuya, K. Mitsuishi, M. Shimojo, K. Kajikawa et al., "Cross-sectional transmission electron microscopy and optical characterization of gold nanoislands," *Japanese Journal of Applied Physics*, vol. 48, Article ID 080207, 2009.

[23] V. Ovchinnikov and A. Shevchenko, "Morphology and surface plasmon resonances of silver nanocomposite layer-by-layer films," *Journal of Nanoscience and Nanotechnology*, vol. 9, no. 6, pp. 3872–3876, 2009.

[24] B. Luk'Yanchuk, N. I. Zheludev, S. A. Maier et al., "The Fano resonance in plasmonic nanostructures and metamaterials," *Nature Materials*, vol. 9, no. 9, pp. 707–715, 2010.

[25] R. R. Naujok, R. V. Duevel, and R. M. Corn, "Fluorescence and Fourier transform surface-enhanced Raman scattering measurements of methylene blue adsorbed onto a sulfur-modified gold electrode," *Langmuir*, vol. 9, no. 7, pp. 1771–1774, 1993.

[26] A. Shevchenko, V. Ovchinnikov, and A. Shevchenko, "Large-area nanostructured substrates for surface enhanced Raman spectroscopy," *Applied Physics Letters*, vol. 100, Article ID 171913, 2012.

Hindawi Publishing Corporation
Journal of Chemistry
Volume 2013, Article ID 679567, 7 pages
http://dx.doi.org/10.1155/2013/679567

Research Article

Barrier Properties and Structural Study of Nanocomposite of HDPE/Montmorillonite Modified with Polyvinylalcohol

María C. Carrera,[1] Eleonora Erdmann,[2] and Hugo A. Destéfanis[1]

[1] *Instituto de Investigaciones para la Industria Química (INIQUI-CONICET), Consejo de Investigaciones (CIUNSa), Facultad de Ingeniería (UNSa), Avenida Bolivia 5150, 4400 Salta, Argentina*
[2] *Instituto Tecnológico de Buenos Aires (ITBA), Instituto de Investigaciones para la Industria Química (INIQUI-UNSa-CONICET), Avenida Eduardo Madero 399, C1106ACD Buenos Aires, Argentina*

Correspondence should be addressed to María C. Carrera; celestecarrera@gmail.com

Received 11 September 2012; Revised 1 February 2013; Accepted 5 February 2013

Academic Editor: Vincenzo Turco Liveri

In this work was studied the permeation of CO_2 in films of high-density polyethylene (HDPE) and organoclay modified with polyvinylalcohol ($MMT_{HDTMA/PVA}$) obtained from melt blending. Permeation study showed that the incorporation of the modified organoclay generates a significant effect on the barrier properties of HDPE. When a load of 2 wt% of $MMT_{HDTMA/PVA}$ was incorporated in the polymer matrix, the flow of CO_2 decreased 43.7% compared to pure polyethylene. The results of TEM showed that clay layers were dispersed in the polymeric matrix, obtaining an exfoliated-structure nanocomposite. The thermal stability of nanocomposite was significantly enhanced with respect to the pristine HDPE. DSC results showed that the crystallinity was maintained as the pure polymeric matrix. Consequently, the decrease of permeability was attributable only to the effect of tortuosity generated by the dispersion of $MMT_{HDTMA/PVA}$. Notably the mechanical properties remain equal to those of pure polyethylene, but with an increase in barrier properties to CO_2. This procedure allows obtaining nanocomposites of HDPE with a good barrier property to CO_2 which would make it competitive in the use of packaging.

1. Introduction

The barrier properties of polymers can be significantly altered by inclusion of impermeable lamellar fillers such as montmorillonites, with sufficient aspect ratio to alter the diffusion path of gas-penetrant molecules. The key issue is to obtain an effective dispersion and exfoliation of the platelets into the polymer matrix to yield a tortuous diffusion pathway for improved barrier properties. In most works concerning nanocomposites, the barrier properties are examined by using gas [1–5] and the literature contains numerous reports on decreased gas permeability [6–20] caused by addition of layered silicates to various polymer matrices.

Enough articles in the literature have focused the studies on nanocomposites made by addition of organoclays, formed from montmorillonite, to thermoplastics using melt-processing techniques [6, 7, 21–26]. This method involves the mixing of the layered silicate with the polymer and heating the mixture above its softening point. Under certain conditions, if the clay layer surfaces are sufficiently compatible with the polymer chains, the polymer can enter between the interlayer spaces, forming an intercalated or exfoliated nanocomposite [27–29]. The incorporation of small amounts (<10 wt%) of clay shows a remarkable influence on the permeability and barrier properties of composite membranes [30].

In the preparation of polymer/clay nanocomposites, is very important the chemical interaction between polymer and clay. For instance, in the case of polyamides and some types of clay, the surface forces are very large due to hydrogen-bond-type interactions; in this case exfoliation is not a difficult process. Nevertheless, in the case of nonpolar polymers like high-density polyethylene (HDPE), there is no good interaction between hydrophilic clays and polymer and the adhesion between them is very poor, resulting in final materials with mechanical and rheological properties well below the pristine polyethylene [31].

To improve the interaction with hydrophobic polymers such as HDPE, the clay is organophilized, increasing polymer/clay affinity and the ability of forming exfoliated nanocomposites [32, 33].

In this work nanocomposites of HDPE and modified clay were prepared by melt blending. The modified clay was obtained in two stages. In the first step the clay was exchanged with hexadecyltrimethylammonium (MMT_{HDTMA}) and in the second step the MMT_{HDTMA} was modified with polyvinyl alcohol (PVA) by in situ polymerization ($MMT_{HDTMA/PVA}$).

In this work was studied the influence of the organoclay modified with PVA on the structure and barrier properties to CO_2 of the nanocomposites. The control CO_2 permeability is of fundamental importance in the selection of materials for food packaging under modified atmosphere (MA), whose principle is to achieve an environment with low concentration of O_2 and high concentration of CO_2 inside the package [34]. Consequently the reduction of CO_2 permeability allows the use of HDPE as a packaging material for many food products. Moreover, the hydrophilic properties of the nanocomposite material make it suitable for use in gas lines, tanks, and pipelines for hydrocarbons [35].

X-ray diffraction (XRD), scanning electron microscopy (SEM), and transmission electron microscopy (TEM) were used to observe the internal structure and morphology of the nanocomposite obtained. The heat stability was studied by thermogravimetric analysis (TGA) and differential scanning calorimetry (DSC).

2. Experimental

2.1. Materials. An HDPE, 40055L from Polisur S.A, with melt flow index of 10 g/10 min (290°C, 21.6 kg) was chosen as a matrix.

Sodium montmorillonite (MMT) clay supplied by Minarmco (CEC = 70 meq/100 g and particle size < 325 mesh), was organically modified with a hexadecyltrimethylammonium bromide salt (MERCK) (HDTMA) following the modified technique of Yeh et al. [33]. The organophilic clay was modified by in situ polymerization: the vinyl acetate monomer (vinyl acetate (VETEC, Brazil)) was intercalated into layer of MMT_{HDTMA} and followed by a free radical polymerization with benzoyl peroxide as an initiator reaction. The polyvinyl acetate/MMT_{HDTMA} solution was saponified by alcoholysis with NaOH solution to obtain polyvinyl alcohol-modified organophilic clay ($MMT_{HDTMA/PVA}$) [36].

2.2. Melt Mixing. Nanocomposites of HDPE with loads of 0.6 wt% and 2 wt% of organoclay modified with PVA were prepared using a mixing chamber Rheomix 600 coupled to a Haake Rheocord 9000 torque rheometer with roller type rotors. The temperature used was 190°C and the speed of work was 90 rpm.

2.3. Characterization. Films for characterization were prepared by compression molding of the nanocomposites using a Carver model hydraulic press, under 27.6 MPa pressure at 190°C for 5 minutes.

X-ray diffraction (XRD) analyses were performed in a Rigaku Miniflex DRX 600 diffractometer using nickel-filtered CuKα radiation operating at 30 kV and 15 mA. The data were recorded at 2θ rate of 2°min^{-1}.

Scanning electron microscopy (SEM) was carried out using a JEOL JSM-6480 LV microscope with an accelerating voltage of 15 kV. Samples were coated with gold in order to study the surface morphology.

The sample for TEM was cut from cry oultramicrotome, RMC Powertome XL at 60 nm thickness with diamond knife at a temperature of −40°C. The sections were transferred into a copper grid. TEM imaging was done using Jeol JEM 2000FX electronic microscope operating at 200 kV accelerating voltage.

2.4. Measurement of Properties. The thermal behavior was carried out using a TA Instrument TGA model Q500 from 30°C to 700°C with a heating rate of $10^{\circ}\text{C}\cdot\text{min}^{-1}$, operating under N_2 flow of $60\ \text{mL}\cdot\text{min}^{-1}$. The melting point and fusion enthalpy were obtained by differential scanning calorimeter, DSC, model Q100, TA Instrument. Samples were heated from 20°C to 200°C at a rate of $10^{\circ}\text{C}\cdot\text{min}^{-1}$ then cooled down to 20°C and heated again at the same rate to 250°C under N_2 atmosphere. The crystallinity data were obtained from the second heating run.

The CO_2 permeation was carried out in an equipment of permeation standard (Permatran C200), at a temperature of 26°C and humidity of 0%. The concentration of CO_2 used was 100% in films of 0.2 mm thickness.

Tensile tests were carried out on seven films of each sample, for using an instron tensile testing machine model 5569 at 23°C and 45% relative humidity, following the ASTM-D882 method. The test was performed at 10 mm/min of strain speed.

3. Results and Discussion

3.1. Morphology and Internal Structure. Figure 1(a) shows XRD of unmodified organoclay (MMT_{HDTMA}), clay modified with PVA ($MMT_{HDTMA/PVA}$), and the modified clay mixed with HDPE 2 wt%. The peak at low angle of 4.6 degree in Figure 1(a) corresponds to the basal reflection (001) of the organoclay (MMT_{HDTMA}). The diffractogram of the sample of $MMT_{HDTMA/PVA}$ shows a disappearance of the peaks between $2\theta = 2^{\circ}$–10°, which would indicate a possible exfoliation, since the PVA chains could have destroyed completely the ordered structure of the clay. In the HDPE/$MMT_{HDTMA/PVA}$ material, with load of 0.6 wt% and 2 wt% (Figure 1(b)) the diffraction peaks were not observed between 2–5 degree, in the XRD diffractograms, either because of a much too large spacing between the layers (i.e., exceeding 8 nm in the case of ordered exfoliated structure) or because the nanocomposite does not present ordering anymore [27].

Figure 2(a) shows the SEM micrograph of the typical morphology of a binary mixture of HDPE and PVA which are incompatible polymers. It shows large PVA particles with poor interfacial adhesion and dispersion in the polyethylene

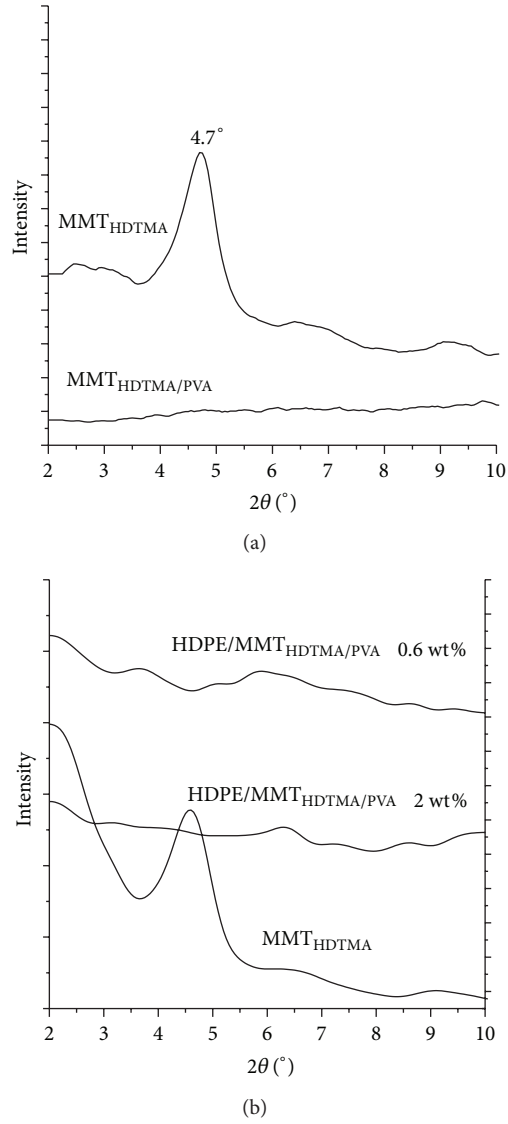

Figure 1: X-ray diffraction curves of (a) MMT_{HDTMA} and $MMT_{HDTMA/PVA}$ and (b) MMT_{HDTMA} and $HDPE/MMT_{HDTMA/PVA}$ with 0.6 wt% and 2 wt%.

matrix. The morphology improves when the load organoclay was increased in the polymer matrix (Figure 2(b)), especially when the loads were high (2 wt%), meaning that, a good dispersion of the clay was obtained in the polymeric matrix.

The TEM image in Figure 3 shows completely different structures having two different loads of $MMT_{HDTMA/PVA}$ in the polymer matrix of polyethylene. When the load is 0.6 wt% the presence of two types of structures (agglomerate) and alternating layers (intercalated) is observed (Figures 3(a)–3(c)). While the XRD of this material ($HDPE/MMT_{HDTMA/PVA}$) was not observed any peak could be the low concentration of clay in the polymer matrix that is not detected by the team and not as previously thought exfoliation in when those results (XRD).

When the load of clay is 2 wt% the material presents an exfoliated structure (Figures 3(d)–3(f)) which is consistent with XRD results (Figure 1(b)).

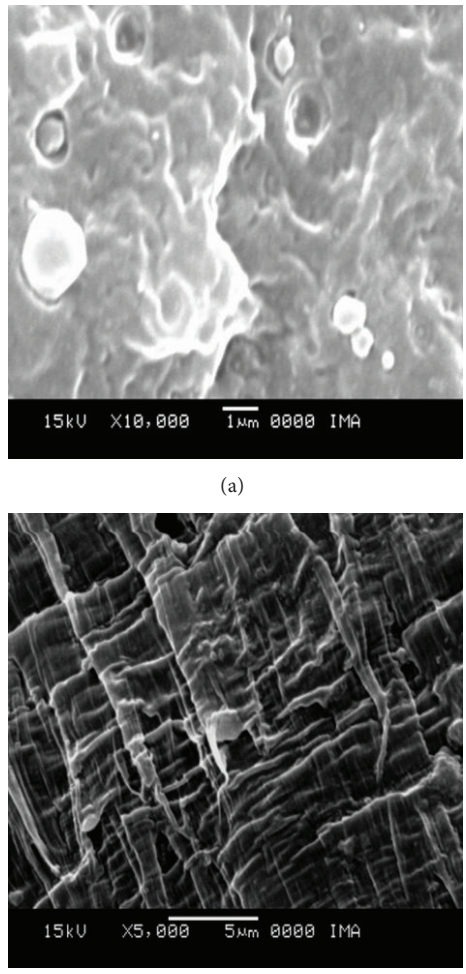

Figure 2: SEM (a) images of $HDPE/MMT_{HDTMA/PVA}$ with 0.6 wt% (a) and 2 wt% (b).

3.2. Thermal Behavior and Crystallinity. Figure 4 shows that, in general terms, in the thermal stability of the HDPE composite materials obtained by TGA only a small change has occurred. The presence of $MMT_{HDTMA/PVA}$ causes a change in the profile of DTGA (Figure 4), because was observed decomposition processes PVA (dehydration: 200°C–400°C) and ammonium salt which occur in the same range.

DSC results of HDPE and $HDPE/MMT_{HDTMA/PVA}$ nanocomposite are shown in Figure 5. The melting point (T_m) of the nanocomposites does not change with regard to pristine HDPE.

The polymers are semicrystalline materials, where crystalline regions are surrounded by amorphous regions, so the properties are influenced by the degree of crystallinity and the size and shape of the crystals. The degree of crystallinity of the samples was calculated using the total enthalpy method [38] from (1), taking the data of enthalpy of fusion of each material (ΔH_m), obtained from the area under the curve of heat versus temperature, Figure 5.

$$\chi_C = \frac{\Delta H_m}{\Delta H_m^0}, \quad (1)$$

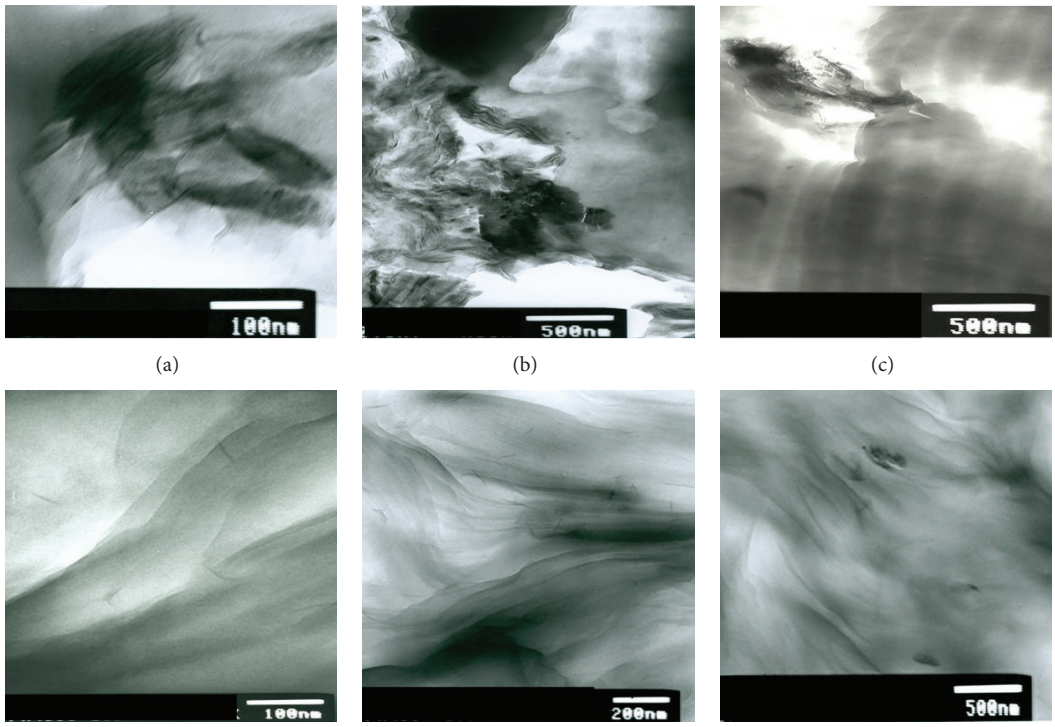

Figure 3: TEM images of HDPE/$MMT_{HDTMA/PVA}$ with 0.6 wt% (X100 (a), X500 (b), and X500 (c)) and 2 wt% (X100 (d), X200 (e), and X500 (f)).

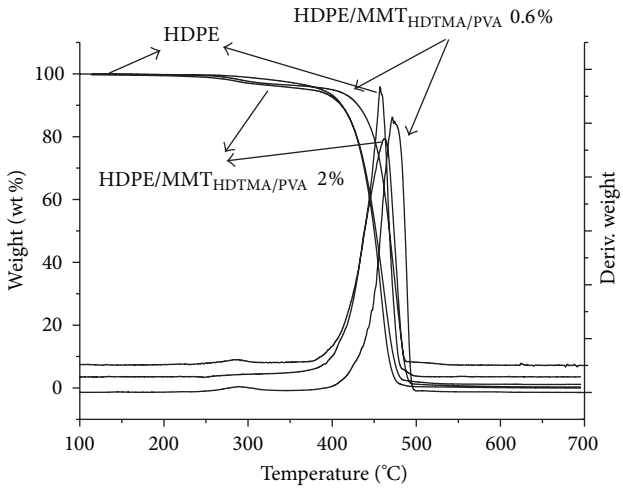

Figure 4: TG and DTG curves of HDPE, HDPE/$MMT_{HDTMA/PVA}$ 0.6 wt%, and HDPE/$MMT_{HDTMA/PVA}$ 2 wt%.

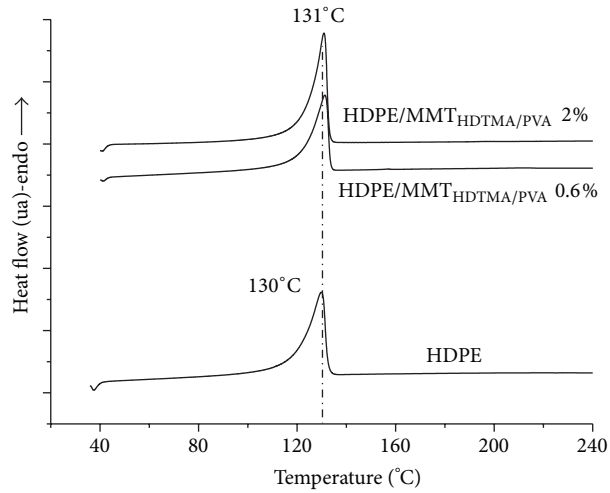

Figure 5: DSC curves of HDPE, HDPE/$MMT_{HDTMA/PVA}$ 0.6 wt%, and HDPE/$MMT_{HDTMA/PVA}$ 2 wt%.

where ΔH_m^0 is the crystalline fusion enthalpy to 100% crystalline polyethylene (ΔH_m^0 = 288 J·g^{-1} [38]) and ΔH_m is the material fusion enthalpy.

In terms ofthe crystallinity of the composite materials shown in Table 1 itis not appreciably changed with respect to the original polymer.

Table 1: Fusion enthalpy and crystalline degree of the materials.

Sample	ΔH_m (J/g)	χ_C (%)
HDPE	156.1	54.2
HDPE/$MMT_{HDTMA/PVA}$ 0.6 wt%	131.8	50
HDPE/$MMT_{HDTMA/PVA}$ 2 wt%	142.0	49.3

Table 2: Mechanical properties of the materials.

Sample	Young's modulus (Mpa)	Yield stress (Mpa)	Yield elongation (%)	Tensile strength (Mpa)
HDPE	745 ± 88	12.1 ± 0.8	2.2 ± 0.4	20.4 ± 1.3
HDPE/$MMT_{HDTMA/PVA}$ (0.6 wt%)	657 ± 74	11.8 ± 0.5	2.3 ± 0.5	18.8 ± 1.8
HDPE/$MMT_{HDTMA/PVA}$ (2 wt%)	623 ± 45	13.9 ± 0.6	3.3 ± 0.6	21.2 ± 0.7

Table 3: CO_2 permeability of HDPE and HDPE/$MMT_{HDTMA/PVA}$ (0.6 wt% and 2 wt%).

Sample	P_{CO_2} ($cm^3 \cdot mm/m^2 \cdot day$)
HDPE	451 ± 22.4
HDPE/$MMT_{HDTMA/PVA}$ 0.6 wt%	553 ± 154
HDPE/$MMT_{HDTMA/PVA}$ 2 wt%	254 ± 25

3.3. Mechanical Properties. Tensile strength and elongations at yield point and at break of these nanocomposites are presented in Table 2. No significant change in these mechanical properties was observed when the modified clay was added to the HDPE.

3.4. Barrier Properties. Considering ideal gas behavior, the flow can be calculated according to (2) and the permeation by (3):

$$J = \frac{dV}{dt} \cdot \frac{1}{A}, \tag{2}$$

$$P = J \cdot e, \tag{3}$$

where A is the area of permeation, V is the volume of gas, t is the time to permeate, P is the permeation, and e is the thickness film.

The CO_2 permeability through the films of HDPE and the composite of HDPE with modified clay were obtained with the (3). Table 3 shows that the CO_2 permeability of material with 2 wt% organoclay modified with PVA decreases 43.7% compared to pure HDPE. With load of 0.6 wt% the permeability was increased 22.5% compared to pristine polyethylene. This behavior can be attributed to the fact that the main transport that controls the mechanism could be the interface polymer/clay and the films of $HDPE/MMT_{HDTMA/PVA}$ (0.6 wt%) with more defects at the interface have less resistance to permeation [39], that is, they do not have the sufficient amount of clay to increase the barrier properties.

The barrier properties were increased as a result of the tortuous path created by a 2 wt% of clay platelets [37]. This behavior can be attributed to a better orientation of the modified clay with an exfoliated structure to form a more tortuous path at the CO_2 diffusion in the membrane. On the other hand the main transport that controls the mechanism could be the interface polymer/clay.

From the results obtained a model was used to calculate the tortuosity. A simple permeability model for a regular arrangement of platelets has been proposed by Nielsen [10]

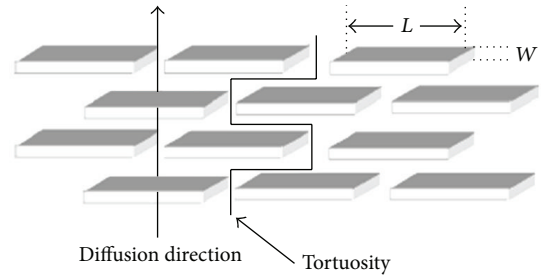

Figure 6: Regular arrangement of orthogonally shaped platelets in a parallel array with their main direction perpendicular to the diffusion direction (reproduced from [37]).

and is presented in Figure 6. The nanoparticles are evenly dispersed and considered to be rectangular platelets with finite width, L, and thickness, W. Their orientation is perpendicular to the diffusion direction [40].

The solubility coefficient of this nanocomposite is

$$S = S_0 (1 - \varphi), \tag{4}$$

where S_0 is the solubility coefficient of the neat polymer and φ is the volume fraction of the nanoplatelets that are dispersed in the matrix. In this approximation the solubility does not depend on the morphological features of the phases.

The platelets act as impermeable barriers to the diffusing molecules, forcing them to follow longer and more tortuous paths in order to diffuse through the nanocomposite. The diffusion coefficient, D, is influenced by the tortuosity, τ:

$$D = \frac{D_0}{\tau}. \tag{5}$$

Therefore a model for calculation of tortuosity is the following:

$$\tau = 1 + \frac{L}{2W}\varphi. \tag{6}$$

Values of mean filler aspect ratio ($\alpha = L/W$) were calculated from a detailed analysis of several TEM images observed in Figures 3(a)–3(f). This values (α) and the tortuosity (τ) are observed in the Table 4.

The medium tortuosity for the nanocomposites with 0.6 wt% is τ_m = 1.15 and 1.33 when the load of clay is 2 wt%. This explains that having substantial tortuosity the diffusivity of nanocomposite decreases with respect to the diffusivity of pure polyethylene and consequently decreases the permeability to CO_2 in the material with 2 wt%.

Table 4: Mean filler aspect ratio (α) and tortuosity of material of HDPE/$MMT_{HDTMA/PVA}$ (0.6 wt% and 2 wt%).

Sample	HDPE/$MMT_{HDTMA/PVA}$ 0.6 wt%			HDPE/$MMT_{HDTMA/PVA}$ 2 wt%		
Figure 3	(a)	(b)	(c)	(d)	(e)	(f)
$\alpha = L/W$	19	11	30	11	15	29
τ	1.14	1.10	1.20	1.20	1.27	1.51
τ_m		1.15			1.33	

4. Conclusion

The organoclay modified with PVA improved the CO_2 barrier properties of HDPE when the load is of 2 wt%, so it is very important to note the following surprising result for the nanocomposite: the flux density decreases about 43.7% as compared with pristine polyethylene. Since the crystallinity of the material is in the order of polyethylene, the decreased of CO_2 permeability is attributable solely to the incorporation of the organophilic clay-modified PVA, allowing a good dispersion of the plates in the polymer matrix. These results are consistent with the exfoliated structure of material obtained. Notably, the mechanical properties of the composite are maintained in the same order of polyethylene which makes it a competitive material with good mechanical properties which characterize the HDPE, but with barrier properties to CO_2 improved 43.7%.

References

[1] Z. Ke and B. Yongping, "Improve the gas barrier property of PET film with montmorillonite by in situ interlayer polymerization," *Materials Letters*, vol. 59, no. 27, pp. 3348–3351, 2005.

[2] O. Gain, E. Espuche, E. Pollet, M. Alexandre, and P. Dubois, "Gas barrier properties of poly(ε-caprolactone)/clay nanocomposites: influence of the morphology and polymer/clay interactions," *Journal of Polymer Science B*, vol. 43, no. 2, pp. 205–214, 2005.

[3] E. Picard, A. Vermogen, J. F. Gérard, and E. Espuche, "Barrier properties of nylon 6-montmorillonite nanocomposite membranes prepared by melt blending: influence of the clay content and dispersion state. Consequences on modelling," *Journal of Membrane Science*, vol. 292, no. 1-2, pp. 133–144, 2007.

[4] S. S. Ray, K. Yamada, M. Okamoto, A. Ogani, and K. Ueda, "New polylactide/layered silicate nanocomposites. 3. High-performance biodegradable materials," *Chemistry of Materials*, vol. 15, no. 7, pp. 1456–1465, 2003.

[5] T. Ogasawara, Y. Ishida, T. Aoki, and T. Ogura, "Helium gas permeability of montmorillonite/epoxy nanocomposites," *Composites A*, vol. 37, no. 12, pp. 2236–2240, 2006.

[6] S. S. Ray and M. Okamoto, "Polymer-layered silicate nanocomposite: a review from preparation to processing," *Progress in Polymer Science*, vol. 28, pp. 1539–1641, 2003.

[7] E. P. Giannelis, "Polymer-layered silicate nanocomposites: Synthesis, properties and applications," *The Applied Organometallic Chemistry*, vol. 12, pp. 675–680, 1998.

[8] E. P. Giannelis, "Polymer layered silicate nanocomposites," *Advanced Materials*, vol. 8, pp. 29–35, 1996.

[9] K. Yano, A. Usuki, and A. Okada, "Synthesis and properties of polyimide-clay hybrid films," *Journal of Polymer Science A*, vol. 35, no. 11, pp. 2289–2294, 1997.

[10] L. E. Nielsen, "Models for the permeability of filled polymers systems," *Journal of Macromolecular Science, Part A*, vol. 1, no. 5, pp. 929–942, 1967.

[11] N. K. Lape, E. E. Nuxoll, and E. L. Cussler, "Polydisperse flakes in barrier films," *Journal of Membrane Science*, vol. 29, pp. 29–37, 2004.

[12] D. Perry, W. J. Ward, and E. L. Cussler, "Unsteady diffusion in barrier membranes," *Journal of Membrane Science*, vol. 44, no. 2-3, pp. 305–311, 1989.

[13] N. K. Lape, C. Yang, and E. L. Cussler, "Flake-filled reactive membranes," *Journal of Membrane Science*, vol. 209, no. 1, pp. 271–282, 2002.

[14] C. Yang, W. H. Smyrl, and E. L. Cussler, "Flake alignment in composite coatings," *Journal of Membrane Science*, vol. 231, no. 1-2, pp. 1–12, 2004.

[15] W. R. Falla, M. Mulski, and E. L. Cussler, "Estimating diffusion through flake-filled membranes," *Journal of Membrane Science*, vol. 119, no. 1, pp. 129–138, 1996.

[16] R. K. Bharadwaj, "Modeling the barrier properties of polymer-layered silicate nanocomposites," *Macromolecules*, vol. 34, no. 26, pp. 9189–9192, 2001.

[17] A. A. Gusev and H. R. Lusti, "Rational design of nanocomposites for barrier applications," *Advanced Materials*, vol. 13, pp. 1641–1643, 2001.

[18] G. H. Fredrickson and J. Bicerano, "Barrier properties of oriented disk composites," *Journal of Chemical Physics*, vol. 110, pp. 2181–2188, 1999.

[19] S. S. Ray, K. Yamada, M. Okamoto, A. Ogami, and K. Ueda, "New polylactide/layered silicate nanocomposites. 3. High-performance biodegradable materials," *Chemistry of Materials*, vol. 15, no. 7, pp. 1456–1465, 2003.

[20] S. S. Ray, K. Okamoto, and M. Okamoto, "Structure-property relationship in biodegradable poly(butylene succinate)/layered silicate nanocomposites," *Macromolecules*, vol. 36, no. 7, pp. 2355–2367, 2003.

[21] H. R. Dennis, D. L. Hunter, D. Chang et al., "Effect of melt processing conditions on the extent of exfoliation in organoclay-based nanocomposites," *Polymer*, vol. 42, no. 23, pp. 9513–9522, 2001.

[22] J. W. Gilman, A. B. Morgan, E. P. Giannelis, M. Wuthenow, and E. Manias, "Flammability and thermal stability studies of polymer layered-silicate (Clay) nanocomposites-II," in *Proceedings of the BCC Conference on Flame Retardancy*, pp. 1–11, 1999.

[23] P. G. Nahin and P. S. Backlund, Union Oil Company, United States patent no. 3, 084, 117, 1936.

[24] R. A. Vaia, H. Ishii, and E. P. Giannelis, "Synthesis and properties of two-dimensional nanostructures by direct intercalation of polymer melts in layered silicates," *Chemistry of Materials*, vol. 5, no. 12, pp. 1694–1696, 1993.

[25] R. A. Vaia, K. D. Jandt, E. J. Kramer, and E. P. Giannelis, "Microstructural evolution of melt intercalated polymer-organically modified layered silicates nanocomposites," *Chemistry of Materials*, vol. 8, no. 11, pp. 2628–2635, 1996.

[26] R. A. Vaia and E. P. Giannelis, "Lattice model of polymer melt intercalation in organically-modified layered silicates," *Macromolecules*, vol. 30, no. 25, pp. 7990–7999, 1997.

[27] M. Alexandre and P. Dubois, "Polymer-layered silicate nanocomposites: preparation, properties and uses of a new

class of materials," *Materials Science and Engineering R*, vol. 28, no. 1, pp. 1–63, 2000.

[28] S. Pavlidoua and C. D. Papaspyrides, "A review on polymer-layered silicate nanocomposites," *Progress in Polymer Science*, vol. 33, pp. 1119–1198, 2008.

[29] P. C. Lebaron, Z. Wang, and T. J. Pinnavaia, "Polymer-layered silicate nanocomposites: an overview," *Applied Clay Science*, vol. 15, no. 1-2, pp. 11–29, 1999.

[30] J. K. Kim, C. Hu, R. S. C. Woo, and M. L. Sham, "Rheology of confined polymer melts under shear flow: strong adsorption limit," *Composites Science and Technology*, vol. 65, p. 805, 2005.

[31] K. Chrissopoulou, I. Altintzi, S. H. Anastasiadis et al., "Controlling the miscibility of polyethylene/layered silicate nanocomposites by altering the polymer/surface interactions," *Polymer*, vol. 46, no. 26, pp. 12440–12451, 2005.

[32] G. Gorrasi, M. Tortora, V. Vittoria et al., "Vapor barrier properties of polycaprolactone montmorillonite nanocomposites: effect of clay dispersion," *Polymer*, vol. 44, no. 8, pp. 2271–2279, 2003.

[33] J. M. Yeh, H. Y. Huang, C. L. Chen, W. F. Su, and Y. H. Yu, "Siloxane-modified epoxy resin-clay nanocomposite coatings with advanced anticorrosive properties prepared by a solution dispersion approach," *Surface and Coatings Technology*, vol. 200, no. 8, pp. 2753–2763, 2006.

[34] J. Welti-Chanes, F. Vergara-Balderas, J. A. Guerrero-Beltrán, R. García Torres, and R. Villa-Rojas, "Métodos, criterios y modelación para la selección de películas plásticas en atmósferas modificadas," in *Segundo Simposio Internacional de Innovación y Desarrollo de Alimentos*, Montevideo, Uruguay, Septiembre 2005.

[35] S. Kenig, A. Ophir, O. Shepelev, and F. Weiner, "High barrier blow molded containers based on Nano Clay Composites," in *Proceedings of the Annual Technical Conference on the Society of Plastics Engineering*, San Francisco, Calif, USA, May 2001.

[36] M. C. Carrera, *Preparación y efecto de los nanocompuestos polímero-arcilla sobre las propiedades de barrera y mecánicas para polímeros hidrocarbonados y biodegradables [Ph.D. thesis]*, Universidad Nacional de Salta, Salta, Argentina, 2011.

[37] K. H. Wang, M. H. Choi, C. M. Koo, Y. S. Choi, and I. Chung, "Synthesis and characterization of maleated polyethylene/clay nanocomposites," *Journal of Polymer*, vol. 42, no. 24, pp. 9819–9826, 2001.

[38] H. A. Khonakdar, J. Morshedian, U. Wagenknecht, and S. H. Jafari, "An investigation of chemical crosslinking effect on properties of high-density polyethylene," *Polymer*, vol. 44, no. 15, pp. 4301–4309, 2003.

[39] C. Lotti, C. S. Isaac, M. C. Branciforti, R. M. V. Alves, S. Liberman, and R. E. S. Bretas, "Rheological, mechanical and transport properties of blown films of high density polyethylene nanocomposites," *European Polymer Journal*, vol. 44, no. 5, pp. 1346–1357, 2008.

[40] G. Choudalakis and A. D. Gotsis, "Permeability of polymer/clay nanocomposites: a review," *European Polymer Journal*, vol. 45, no. 4, pp. 967–984, 2009.

Hindawi Publishing Corporation
Journal of Chemistry
Volume 2013, Article ID 250760, 6 pages
http://dx.doi.org/10.1155/2013/250760

Research Article

Preparation and Electrocatalytic Characteristics Research of Pd/C Catalyst for Direct Ethanol Fuel Cell

Qiao Xia Li, Ming Shuang Liu, Qun Jie Xu, and Hong Min Mao

Shanghai Key Laboratory of Colleges and Universities for Corrosion Control in Electric Power System and Applied Electrochemistry, Shanghai University of Electric Power, Shanghai 200090, China

Correspondence should be addressed to Qun Jie Xu; xuqunjie@shiep.edu.cn

Received 31 October 2012; Revised 7 January 2013; Accepted 21 January 2013

Academic Editor: Valeria La Parola

Two kinds of carbon-support 20% Pd/C catalysts for use in direct ethanol fuel cell (DEFC) have been prepared by an impregnation reduction method using $NaBH_4$ and NaH_2PO_2 as reductants, respectively, in this study. The catalysts were characterized by XRD and TEM. The results show that the catalysts had been completely reduced, and the catalysts are spherical and homogeneously dispersed on carbon. The electrocatalytic activity of the catalysts was investigated by electrochemical measurements. The results indicate that the catalysts had an average particle size of 3.3 nm and showed the better catalytic performance, when $NaBH_4$ was used as the reducing agent. The electrochemical active surface area of Pd/C ($NaBH_4$) was 56.4 $m^2 \cdot g^{-1}$. The electrochemical activity of the Pd/C ($NaBH_4$) was much higher than that of Pd/C (NaH_2PO_2).

1. Introduction

Nowadays, great attention has been paid to direct alcohol fuel cell (DAFC) as portable applications due to some superior advantages over analogous devices fed with hydrogen. Direct ethanol fuel cell (DEFC) has attracted attention, since ethanol has no toxicity comparing to methanol and can be easily produced in great quantities by the fermentation of sugar-containing raw materials [1, 2]. The electroactivity of anodic materials is one of the main factors influencing the practical application of DAFC. Although platinum electrodes present efficient catalytic activity for alcohol oxidation, the widely practical application of Pt electrodes as anodes in DAFC is limited by the high cost of the metal platinum. If DAFC could be operated in an alkaline instead of an acidic electrolyte, it is easy to consider that the kinetics of fuel cells will be significantly improved and Pt-free electrocatalysts can be used. It is reported that Pd is a good electrocatalyst for ethanol oxidation and showed higher activity than that of Pt in alkaline media [3, 4].

Recently, nanoparticle palladium has recently received much attention due to some distinguished advantages of it such as significantly large surface areas and high stability. Wen et al. [5] prepared Pd/SnO_2-GNS catalysts by a microwave-assisted reduction process. It was found that, compared with Pd/GNS, the Pd/SnO_2-GNS catalyst showed superior electrocatalytic activity for ethanol oxidation. The interest in Pd not only is for the purpose to lower the cost of catalysts but pursuits an improved catalytic activity. One method to promote the catalytic activity of Pd is alloying with another metal, such as Ag and Sn [6–9]. Liu et al. [10] synthesized PdNi nanoparticles by a chemical reduction process with formic acid. Zhou et al. [11] studied the electrooxidation of ethanol on a polycrystalline Pd disk electrode in alkaline media in situ Fourier transform infrared (FTIR) reflection spectroscopy. The selectivity for ethanol oxidation to CO_2 (existing as CO_3^{2-} in alkaline media) was determined as low as 2.5% in the potential region where Pd electrode exhibited considerable electrocatalytic activity (−0.60 to 0.0 V versus SCE). Nevertheless, the ability of Pd for breaking C–C bond in ethanol is still slightly better than that of Pt under the same conditions.

In the present work, we prepared two different nanoparticle Pd/C electrocatalysts using $NaBH_4$ and NaH_2PO_2 as reductants, respectively, to investigate the nanoparticle palladium towards ethanol oxidation reaction (EOR) in alkaline

solution. In addition, we have also probed the electrochemical properties of the electrocatalysts to explore their potential applications in DEFC.

2. Experimental

2.1. Instrumentation. XRD patterns were collected using a Bruker D8-Advance Powder X-ray diffractometer (Cu KR radiation, wavelength 1.5418 Å). Transmission electron microscopy (TEM) images were characterized with a JEM-2100F HR-TEM model using an accelerating voltage of 80 and 200 KV. 10.0 mg catalyst was dissolved in aqua regia (a strong acid mixture with $HCl : HNO_3$ volume ratio of 3 : 1) to form a Pd aqueous solution, and ICP-AES was performed to detect the catalyst metal loading. All electrochemical measurements were performed in a standard three-electrode cell using a CHI 660C Electrochemical Analyzer.

2.2. Reagents and Solutions. All reagents used were of high purity and analytical reagent grade. $PdCl_2$ was purchased from the Shanghai Institute of Fine Chemical Materials (China); Vulcan XC-72 was supplied by Cabot Co. Ltd. (USA); Sodium borohydride (96%, $NaBH_4$), Sodium hypophosphite hydrate ($NaH_2PO_2{\cdot}H_2O$), Trisodium citrate dehydrate ($C_6H_5Na_3O_7{\cdot}2H_2O$) ethanol, and ethylene glycol were from Sinopharm Chemical Reagent Co. Ltd. 5% Nafion solution was from DuPont Co. Ltd (USA); all other reagents were of analytical grade and used without further purification. The water utilized in all studies was double distilled and deionized.

2.3. Catalyst Preparation. XC-72 carbon was treated in 5 M HNO_3 solution with vigorous stirring. 40.0 mg of the prepared carbon and 2 mmol L^{-1} $PdCl_2$ aqueous solution were added in a mixture of deionized water and ethylene glycol (V/V, 3 : 1). The mixture was stirred for 1 h. After that, the appropriate amount of $C_6H_5Na_3O_7 \cdot 2H_2O$ was added into the mixture as stabilizing agent and then put into an ultrasonic bath, keeping the temperature at 50°C for 0.5 h in continuous ultrasonic concussion. Subsequently, adjust pH to 11 using 1 M NaOH aqueous solution; excess amounts of 0.01 M $NaBH_4$ (freshly prepared) were added into the mixtures dropwise. After being stirred for 6 h at 50°C, the mixture was filtered and washed several times with deionized water to completely remove all excess reducing agents. The remaining solids were dried in a vacuum oven for 24 h at 80°C. The final catalyst was Pd/C ($NaBH_4$). Pd/C (NaH_2PO_2) was prepared by the similar method using Sodium hypophosphite hydrate as a reducing agent. The weight percentage of Pd was 20% in both catalysts.

2.4. Electrochemical Measurements. Cyclic voltammetry (CV) and chronoamperometry measurements were collected in 1 M KOH + 1 M ethanol solution at a scan rate of 50 $mV{\cdot}s^{-1}$. The working electrodes were prepared by dropping 4 μL of the electrocatalyst onto glassy carbon electrode (GCE, 0.07 cm^2). The ink was prepared by ultrasonically mixing 5 mg of electrocatalyst sample in a mixture of 1 mL of ethanol and 120 μL of 5% Nafion solution. The counter electrode was large Pt foils, and the reference electrode was saturated calomel electrode (SCE). The CV tests were carried out in the potential range of −0.8 to 0.4 V. Before experiments, pure nitrogen gas (99.99%) was bubbled through the solution at the last 30 min to remove the dissolved oxygen in the solution. CO striping voltammetric measurements were performed as follows: after purging the solution with N_2 for 30 min, gaseous CO was bubbled for 30 min to form CO adlayer on catalysts while maintaining potential at −0.6 V. Excess CO in solution was purged with N_2 for 2 h and CO stripping voltammetry was recorded in 1 M KOH at 50 $mV{\cdot}s^{-1}$. All experiments were carried out at ambient temperature (~25°C).

3. Results and Discussion

3.1. TEM. Figure 1 shows typical TEM images of the Pd/C ($NaBH_4$) and Pd/C (NaH_2PO_2) catalysts. The catalysts prepared by the reduction method are spherical and homogeneously dispersed on Vulcan XC-72 with no remarkable observation of agglomerations. The average diameters of both catalysts are also summarized in Table 1. They are 3.3 and 38.0 nm for Pd/C ($NaBH_4$) and Pd/C (NaH_2PO_2). Obviously, Pd/C ($NaBH_4$) has a smaller particle size than Pd/C (NaH_2PO_2).

3.2. XRD. The X-ray diffraction (XRD) patterns of the Pd/C ($NaBH_4$) and Pd/C (NaH_2PO_2) catalysts are shown in Figure 2. Sharp and well-defined peaks of Pd/C (NaH_2PO_2) are observed at 2θ values of 40.14°, 46.69°, 68.17°, 82.17°, and 86.69°corresponding to planes of (1 1 1), (2 0 0), (2 2 0), (3 1 1), and (2 2 2), respectively, according to JCPDS No.65-6174. The strong diffraction peaks of Pd/C ($NaBH_4$) are also found in the same angles, but the plane of (2 2 2) disappears. Combined with the TEM images, it is indicated that the crystalline structure of palladium was obtained, respectively, using $NaBH_4$ and NaH_2PO_2 as reductants.

The average particle size of the nanoparticles (d) was estimated by using Scherrer equation (1) after background subtraction from (1 1 1) peak at 2θ of ~40° [12]:

$$d = \frac{k\lambda}{\beta \cos\theta}, \quad (1)$$

where k is the coefficient, generally taken as 0.9, λ is wavelength of X-ray radiation equal to 1.5418 Å, β is full width at half maximum (FWHM) measured in radians, and θ is the angle measured at the position of platinum peaks. Table 1 shows the crystalline size of the electrocatalysts.

3.3. Electrochemical Measurements. Cyclic voltammetry was used to quantify the electrocatalytic activities of the Pd/C as prepared for room temperature. Figure 3 shows the CV results of Pd/C ($NaBH_4$) and Pd/C (NaH_2PO_2) in 1 $mol{\cdot}L^{-1}$ C_2H_5OH + 1 $mol{\cdot}L^{-1}$ KOH solution. The scan rate was selected at 50 $mV{\cdot}s^{-1}$ in the potential range from −0.8 to 0.4 V. The oxidation peak in the forward scan is corresponding to the oxidation of freshly chemisorbed species coming from ethanol adsorption. At a higher potential, the formation of

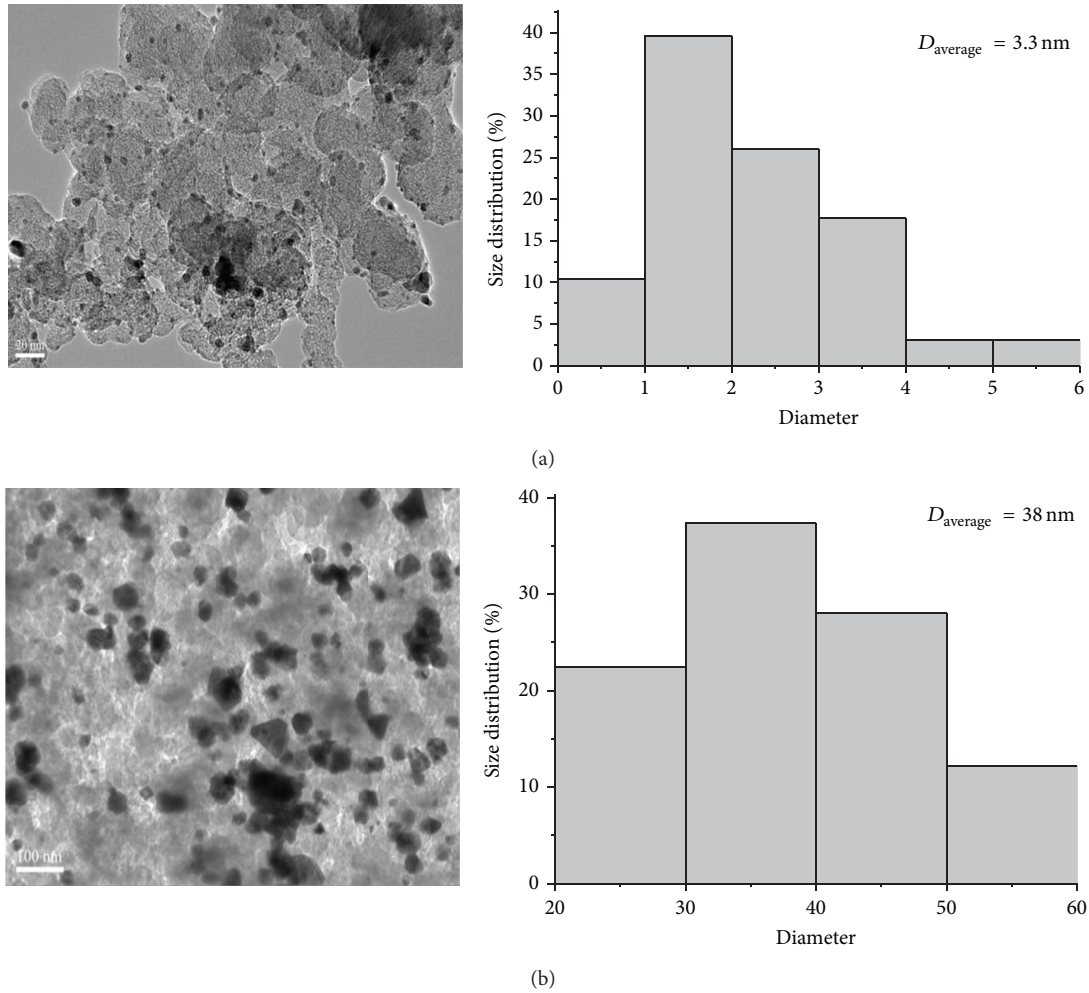

Figure 1: TEM images and particle size distributions of Pd/C ($NaBH_4$) (a) and Pd/C (NaH_2PO_2) (b).

Table 1: Summary of physical properties of Pd/C ($NaBH_4$) and Pd/C (NaH_2PO_2) catalysts.

Catalyst	Pd metal loading detected by ICP-AES	Diameter calculated form XRD/nm	Diameter measured by TEM/nm
Pd/C ($NaBH_4$)	21.6%	2.8	3.3
Pd/C (NaH_2PO_2)	23.8%	3.4	38.0

PdO will block further adsorption of reactive species and lead to a remarkable decrease in current. During the negative-going sweep, the previously formed PdO will be reduced to catalytic active Pd, thus, leading to the recovery of EOR current. Corresponding reactions are shown in (2) and (3) [13]:

$$Pd + C_2H_5OH + 3OH^- \longleftrightarrow Pd\text{-}CH_3CO_{ads} + 3H_2O + 3e \quad (2)$$

$$Pd\text{-}CH_3CO_{ads} + Pd\text{-}OH_{ads} + OH^- \longrightarrow 2Pd + CH_3COO^- + H_2O \quad (3)$$

It is observed from Figure 3 that the current density on Pd/C ($NaBH_4$) is obviously higher, compared with that on Pd/C (NaH_2PO_2). It shows that the Pd/C ($NaBH_4$) catalyst has a better catalytic activity. In the forward scan, the onset potential (E_{onset}) of Pd/C ($NaBH_4$) is −0.544 V, which have negatively shifts by ~30 mV as compared to that of Pd/C (NaH_2PO_2) (−0.516 V). The peak current densities are 28.8 and 17.4 $mA{\cdot}cm^{-2}$ (the area is the surface area of the electrode) for Pd/C ($NaBH_4$) and Pd/C (NaH_2PO_2), respectively, while their peak potentials are −0.258 and −0.232 V. The following parameters, including the E_{onset}, the forward peak potential (E_p), and the forward peak current intensity (j_p) expressed in $mA{\cdot}cm^{-2}$, are shown in Table 2. At the same time, the peak current density of Pd/C ($NaBH_4$) is higher than that of Pd/C in [7, 14].

When compared to NaH_2PO_2 reduction method, the $NaBH_4$ reduction method shows a great advantage in improving the EOR activity. The main reason is that $NaBH_4$ exhibits a higher reduction rate; it is beneficial to maintain high saturation degree during the nucleation stage at the beginning of reaction. On the other hand, the concentrations of BH_4^- and $H_2PO_2^-$ decide the reduction ability of $NaBH_4$ and

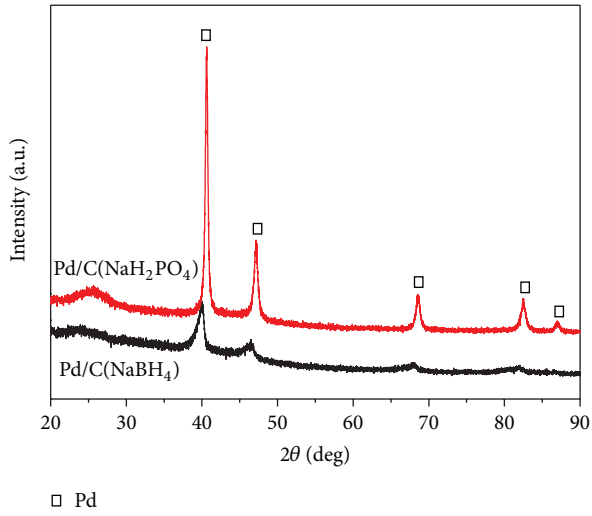

Figure 2: XRD patterns of Pd/C ($NaBH_4$) and Pd/C (NaH_2PO_2).

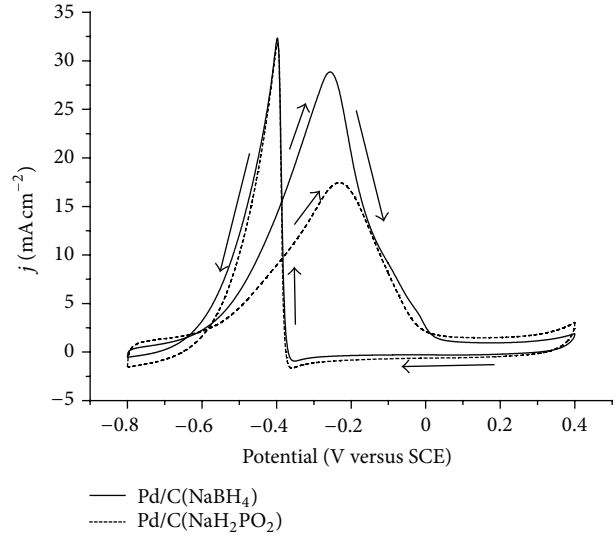

Figure 3: Voltammetric curves of Pd/C ($NaBH_4$) and Pd/C (NaH_2PO_2) in 1 mol·L^{-1} C_2H_5OH + 1 mol·L^{-1} KOH solution.

Table 2: Comparison of activity of ethanol oxidation between Pd/C ($NaBH_4$) and Pd/C (NaH_2PO_2) catalysts.

Catalyst	E_{onset}/V	E_p/V	j_p/mA·cm^{-2}	EASA/ $m^2 \cdot g^{-1}$
Pd/C ($NaBH_4$)	−0.544	−0.258	28.8	56.4
Pd/C (NaH_2PO_2)	−0.516	−0.232	17.4	51.2

NaH_2PO_2, respectively. In alkaline condition, the hydrolysis of BH_4^- is inhibited, (4), but the hydrolysis of $H_2PO_2^-$ is promoted, (5):

$$BH_4^- + 2H_2O = BO_2^- + 4H_2 \uparrow \quad (4)$$

$$H_2PO_2^- + OH^- = HBO_2^{2-} + H_2 \uparrow \quad (5)$$

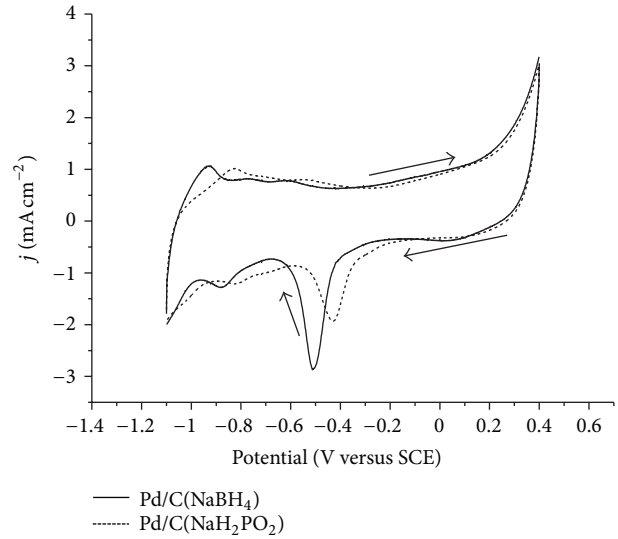

Figure 4: Voltammetric curves of Pd/C ($NaBH_4$) and Pd/C (NaH_2PO_2) in 1 mol·L^{-1} KOH solution.

The cyclic voltammetry of Pd/C ($NaBH_4$) and Pd/C (NaH_2PO_2) in the absence of ethanol is shown in Figure 4. It is observed from Figure 4 that they exhibit significantly high anodic and cathodic current densities. The oxidation peak at lower anodic potential during the forward scan is ascribed to the formation of the adsorbed hydroxyl OH_{ads} while this at high positive potential is related to the formation of Pd oxides [15, 16]. On the cathodic scan, the palladium oxide layers are reduced, with reduction peaks at −0.512 and −0.431, respectively. The potential region from −1.1 to −0.7 V versus SCE on the CV curve of the catalyst is associated with the hydrogen adsorption/desorption. The electrochemical active surface areas (EASA) of catalysts were measured by integrating the charge on hydrogen adsorption-desorption regions by cyclic voltammetry. These values given in Table 1 can be calculated after the deduction of the double layer region on the CV curves represents the charge passed for the hydrogen desorption. The electrochemical active surface areas (EASA) for Pd/C ($NaBH_4$) and Pd/C (NaH_2PO_2) were calculated to be 56.4 and 51.2 $m^2 \cdot g^{-1}$, respectively (Table 2). Obviously, Pd/C ($NaBH_4$) shows a better electrochemical activity because of higher EASA.

In order to evaluate the stability of the catalysts, chronoamperometry was employed and results are shown in Figure 5. The present results show that the current densities represent less decay at the applied constant potentials for a long duration (3600 s). It can be observed that the current densities on the Pd/C ($NaBH_4$) and Pd/C (NaH_2PO_2) after 3600 s are 0.6 and 0.1 mA·cm^{-2}, indicating that the Pd/C ($NaBH_4$) exhibits a better stable electrocatalytic activity towards ethanol oxidation in the alkaline media than Pd/C (NaH_2PO_2). The results are in accordance with the CV results.

CO striping voltammetric curves are shown in Figure 6. The CO striping measurements are conducted in 1 M KOH.

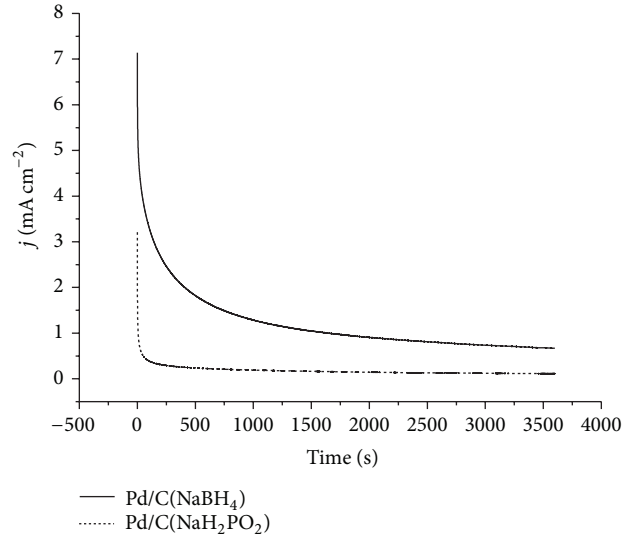

Figure 5: Chronoamperometry curves of Pd/C ($NaBH_4$) and Pd/C (NaH_2PO_2) in 1 mol·L^{-1} C_2H_5OH + 1 mol·L^{-1} KOH solution at a fixed potential of −300 mV for 3600 s.

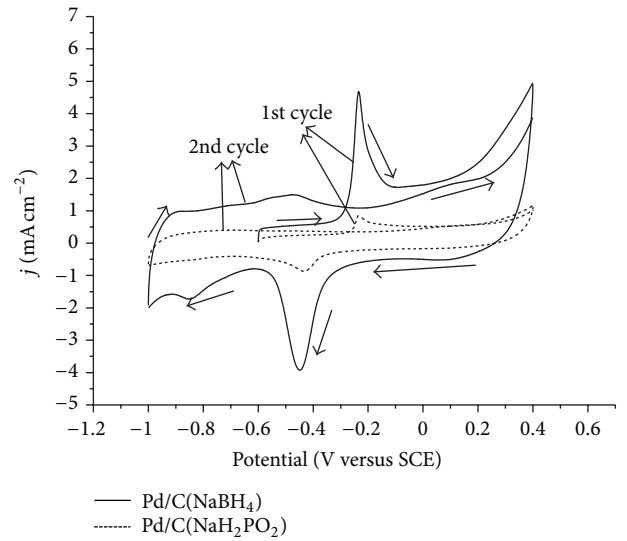

Figure 6: CO striping voltammetric curves of Pd/C ($NaBH_4$) and Pd/C (NaH_2PO_2) in 1 mol·L^{-1} KOH solution.

It is observed from Pd/C ($NaBH_4$) (solid line) that an anodic peak with a shoulder an the high potential side appears in the potential from −0.3 to −0.1 V. In contrast to Pd/C ($NaBH_4$), the Pd/C (NaH_2PO_2) (dash line) possesses a smaller CO stripping peak, indicating that a less amount of CO molecules adsorb on the active surface of Pd/C (NaH_2PO_2). Moreover, the simple and sharp line profile of the stripping peak observed for the Pd/C ($NaBH_4$) demonstrates that the structure of the sample is relatively homogeneous [17]. After stripping, sharp peaks of two CV curves are disappeared in the 2nd cycle. It indicates that the CO preadsorbed on the surface of electrocatalysts is thoroughly oxidized in the first potential scan and the active sites on the Pd surface recover again.

CO has been commonly identified as an intermediate, and the major poisonous species in the alcohol oxidation process, that is prone to adsorb on the surface active sites of electrocatalysts, has been widely used as an effective method to evaluate the active surface area of electrocatalysts [18].

4. Conclusions

In summary, two different 20 wt% nanoparticle Pd/C electrocatalysts were prepared with $NaBH_4$ and NaH_2PO_2 as reductants, respectively. Pd/C ($NaBH_4$) catalysts have small average diameter (3.3 nm) and large electrochemical surface areas (56.4 $m^2 \cdot g^{-1}$). Therefore, Pd/C ($NaBH_4$) exhibits higher reactivity toward EOR in alkaline electrolyte, compared to Pd/C (NaH_2PO_2). The CV tests show that the E_{onset} on Pd/C ($NaBH_4$) is more negative than that of Pd/C (NaH_2PO_2); the peak current densities of Pd/C ($NaBH_4$) (28.8 mA·cm^{-2}) are higher than those of Pd/C (NaH_2PO_2) (17.4 mA·cm^{-2}). After a 3600 s chronoamperometry test at −0.3 V, Pd/C ($NaBH_4$) exhibits a better stable electrocatalytic activity towards ethanol oxidation in the alkaline media than Pd/C (NaH_2PO_2).

Acknowledgments

This project was supported by the National Science Foundation of China (21103107), Innovation Program of Shanghai Municipal Education Commission, China (09YZ339, 10ZZ116), Key Project of Shanghai Committee of Science and technology, China (09230501400, 10160502300), and Talent Development Fund of Shanghai, China.

References

[1] E. M. Cunha, J. Riberto, K. B. Kokoh, and A. R. de Anerade, "Preparation, characterization and application of Pt-Ru-Sn/C trimetallic electro-catalysts for ethanol oxidation in direct fuel cell," *International Journal of Hydrogen Energy*, vol. 36, no. 17, pp. 11034–11042, 2011.

[2] B. R. Tao, J. Zhang, S. C. Hui, X. J. Chen, and L. J. Wan, "An electrochemical methanol sensor based on a Pd–Ni/SiNWs catalytic electrode," *Electrochimica Acta*, vol. 55, no. 17, pp. 5019–5023, 2010.

[3] T. Ogi, R. Honda, K. Tamaoki, N. Saitoh, and Y. Konishi, "Direct room-temperature synthesis of a highly dispersed Pd nanoparticle catalyst and its electrical properties in a fuel cell," *Powder Technology*, vol. 205, no. 1–3, pp. 143–148, 2011.

[4] C. Mahendiran, T. Maiyalagan, K. Scott, and A. Gedanken, "Synthesis of a carbon-coated NiO/MgO core/shell nanocomposite as a Pd electro-catalyst support for ethanol oxidation," *Materials Chemistry and Physics*, vol. 128, no. 3, pp. 341–347, 2011.

[5] Z. L. Wen, S. D. Yang, Y. Y. Liang et al., "The improved electrocatalytic activity of palladium/graphene nanosheets towards ethanol oxidation by tin oxide," *Electrochimica Acta*, vol. 56, no. 1, pp. 139–144, 2010.

[6] J. Kim, T. Momma, and T. Osaka, "Cell performance of Pd–Sn catalyst in passive direct methanol alkaline fuel cell using anion

exchange membrane," *Journal of Power Sources*, vol. 189, no. 2, pp. 999–1002, 2009.

[7] M. C. Oliveira, R. Rego, L. S. Fernandes, and P. B. Tavares, "Evaluation of the catalytic activity of Pd–Ag alloys on ethanol oxidation and oxygen reduction reactions in alkaline medium," *Journal of Power Sources*, vol. 196, no. 15, pp. 6092–6098, 2011.

[8] Y. Wang, Z. M. Sheng, H. Yang, S. P. Jiang, and C. M. Li, "Electrocatalysis of carbon black- or activated carbon nanotubes-supported Pd–Ag towards methanol oxidation in alkaline media," *International Journal of Hydrogen Energy*, vol. 35, no. 19, pp. 10087–10093, 2010.

[9] Y. W. Tang, S. Cao, Y. Chen et al., "Effect of Fe state on electrocatalytic activity of Pd–Fe/C catalyst for oxygen reduction," *Applied Surface Science*, vol. 256, no. 13, pp. 4196–4200, 2010.

[10] Z. L. Liu, X. H. Zhang, and L. Hong, "Physical and electrochemical characterizations of nanostructured Pd/C and PdNi/C catalysts for methanol oxidation," *Electrochemistry Communications*, vol. 11, no. 4, pp. 925–928, 2009.

[11] Z. Y. Zhou, Q. Wang, J. L. Lin, N. Tian, and S. G. Sun, "In situ FTIR spectroscopic studies of electrooxidation of ethanol on Pd electrode in alkaline media," *Electrochimica Acta*, vol. 55, no. 27, pp. 7995–7999, 2010.

[12] V. Radmilovic, H. A. Gasteiger, and P. N. Ross, "Structure and chemical composition of a supported Pt-Ru electrocatalyst for methanol oxidation," *Journal of Catalysis*, vol. 154, no. 1, pp. 98–106, 1995.

[13] Q. F. Yi, F. J. Niu, and L. Z. Sun, "Fabrication of novel porous Pd particles and their electroactivity towards ethanol oxidation in alkaline media," *Fuel*, vol. 90, no. 8, pp. 2617–2623, 2011.

[14] Y. Wang, T. S. Nguyen, X. W. Liu, and X. Wang, "Novel palladium-lead (Pd–Pb/C) bimetallic catalysts for electrooxidation of ethanol in alkaline media," *Journal of Power Sources*, vol. 195, no. 9, pp. 2619–2622, 2010.

[15] Z. Y. Zhang, L. Xin, K. Sun, and W. Z. Li, "Pd–Ni electrocatalysts for efficient ethanol oxidation reaction in alkaline electrolyte," *International Journal of Hydrogen Energy*, vol. 36, no. 20, pp. 12686–12697, 2011.

[16] A. Maghsodi, M. R. M. Hoseini, M. D. Mobarakeh et al., "Exploration of bimetallic Pt-Pd/C nanoparticles as an electrocatalyst for oxygen reduction reaction," *Applied Surface Science*, vol. 257, no. 15, pp. 6353–6357, 2011.

[17] M. Hara, U. Linke, and T. Wandlowski, "Preparation and electrochemical characterization of palladium single crystal electrodes in 0.1 M H_2SO_4 and $HClO_4$—part I: low-index phases," *Electrochimica Acta*, vol. 52, no. 18, pp. 5733–5748, 2007.

[18] Y. J. Huang, X. C. Zhou, J. H. Liao, C. P. Liu, T. H. Lu, and W. Xing, "Preparation of Pd/C catalyst for formic acid oxidation using a novel colloid method," *Electrochemistry Communications*, vol. 10, no. 4, pp. 621–624, 2008.

Hindawi Publishing Corporation
Journal of Chemistry
Volume 2013, Article ID 848205, 5 pages
http://dx.doi.org/10.1155/2013/848205

Research Article

Synthesis and Characterization of Anatase Titanium Dioxide Nanoparticles Using Egg White Solution via Sol-Gel Method

Samira Bagheri,[1] Kamyar Shameli,[1,2] and Sharifah Bee Abd Hamid[1]

[1] *Centre for Research in Nanotechnology & Catalysis (NANOCEN), University of Malaya, IPS Building, 50603 Kuala Lumpur, Malaysia*
[2] *Department of Chemistry, Faculty of Science, Universiti Putra Malaysia, 43400 Serdang, Selangor, Malaysia*

Correspondence should be addressed to Samira Bagheri; samira_bagheri@siswa.um.edu.my

Received 22 September 2012; Revised 8 October 2012; Accepted 23 October 2012

Academic Editor: Fabio Finocchi

Anatase titanium dioxide nanoparticles (TNPs) are synthesized by a simple and cost-effective process with and without freshly water-soluble egg white proteins (albumin) via sol-gel method. The main advantage of using egg white proteins as a gelling agent is that it can provide long-term stability for nanoparticles by preventing particles agglomeration. The X-ray diffraction and FTIR results indicate that the synthesized nanoparticles have only the anatase structure without the presence of any other phase impurities. Additionally, the TNPs are characterized by a number of techniques such as thermogravimetric analysis (TGA), X-ray diffraction analysis (XRD), transmission electron microscopy (TEM), Fourier transform infrared spectroscopy (FTIR), and ultraviolet visible spectra (UV-vis). The sizes of titanium dioxide nanoparticles with and without using egg white solution are 12.55 ± 3.42 nm and 21.45 ± 4.21 nm, respectively. The results indicate that egg white solution is a reliable and cheap green gelling agent that can be used as a matrix in the sol-gel method to synthesis tiny size TNPs.

1. Introduction

Recently, titanium dioxide (TiO_2) has proven to be one of the promising *n*-type semiconductors because of its wide band gap (3.2 eV) under ultraviolet light [1]. In addition, having high physical and chemical stability as well as high refractive index makes this material widely researched [2, 3]. Due to its optical and electronic properties, it can be used in several fields such as photocatalyst, solar cells, sensors, self-cleaning, and bactericidal action [4–6].

Three types of crystallographic structures have been discovered for titanium dioxide including anatase (tetragonal), rutile (tetragonal), and brookite (orthorhombic). Among the structures, rutile is the most stable one while anatase and brookite are metastable phases at ambient temperature. However, due to the large surface area per unit mass and volume, anatase appears to have the highest photocatalytic activity compared to the others [7]. The anatase crystal itself also presents a finer transparency under near *ultraviolet* compared to rutile [8]. Furthermore, the low crystal lattice packing fraction causes anatase crystal to have low hardness and reduces its refractive indices. Therefore, it is preferable in some applications.

Numerous methods were introduced to synthesize TNPs. Some researchers suggest the microemulsion method due to its short processing time [9]. By using the physical vapor deposition (PVD) method, materials are condensed after evaporated to form solid [10]. Other methods such as hydrolysis [11] and hydrothermal [12, 13] have been used in many studies. As for sol-gel method, the materials undergo hydrolysis and polycondensation processes to form the sol and then gel will be formed after aging or gelation and eventually become solid crystals after drying. This can be a simple method as it requires low temperature and controllable final product properties [14–16].

The small size of titanium dioxide nanoparticles can be obtained by using an appropriate gelling agent in the sol-gel method. Egg white proteins (albumin) are famous for their gelling, foaming, and emulsifying characteristics, in addition to their high nutrition quality [17–19]. Because of its solubility in water and its ability to associate with metal ions in solution, egg white has been used as a binder cum

gel forming material in forming the shape of porous ceramics and bulks [20–22].

In this study a simple, costeffective, and environment friendly synthesis introduced to synthesize anatase TNPs by using water-soluble egg white proteins as a gelling agent via sol-gel method. The gelling agent will help to control the nanoparticles size and dispersion due to the expansion during calcination. Furthermore, the surface morphology and size of the anatase titanium dioxide nanoparticles were identified and analyzed by using different apparatus.

2. Experimental Procedures

2.1. Preparation of Anatase TiO_2 Nanoparticles. Sample A as a precursor solution to synthesis TNPs without using egg white solution was prepared when titanium (IV) isopropoxide (98%, Acros Organics) was dissolved in the glacial acetic acid (100%, Merck), it acts as a catalyst to prevent titanium isopropoxide from the nucleophilic's attacks by the water [23] and deionised water (18.2 MΩ cm) with the molar ratio of 1 : 10 : 200. The solution was stirred for several hours and dried at about 80°C overnight. The dried gel was grinded and calcined in a muffle furnace at 500°C for 5 hours. To synthesize sample B of TNPs with egg white solution, the precursor solution was prepared as above mentioned. Freshly water-soluble egg white proteins (30 mL) were homogenized in water (100 mL) by stirring on a magnetic stirrer. Then, the egg white solution was added dropwise into the precursor solution. The solution was continued to be heated and stirred at about 80°C for 5 hours. The result solution was then dried in the oven at 80°C overnight. The dried crystal was grinded and calcined at 500°C for 5 hours.

2.2. Characterization of TiO_2 Nanoparticles. The dried fine gel of synthesized TiO_2 was subjected to thermogravimetric analysis (TGA) (Mettler Toledo TGA/*SDTA 851e*) in order to measure the thermal stability of the materials. Bruker-D8 Advance Powder X-ray diffraction (XRD) was used to determine the crystal phase identification and estimate the crystallite size. To measure the particle size and morphology of TNPs, transmission electron microscopy (TEM), LEO-Libra 120 and scanning electron microscopy (SEM), and *Zeiss* Supra 35VP were used. Fourier transform infrared spectroscopy (FTIR) studies were carried out in the 400–4000 cm^{-1} frequency range. For the infrared absorption spectra, the samples were formed into pellets with KBr and the spectra were recorded on a BRUKER FTIR Spectrometer. IR spectroscopy in the transmission mode gives qualitative information about the way in which the adsorbed molecules are bonded to the surfaces as well as the structural information of solids. For UV-visible absorption spectrum, samples were dispersed in distilled water and sonicated ultrasonically for the absorption studies on a Mettler Toledo spectrophotometer.

3. Results and Discussion

In this study, egg white solution was applied as a stabilizer and gelling agent for reducing agglomeration of nanoparticles. Water-soluble proteins of egg white forms a matrix of entangled polymeric chains, inside the cavities of which can trap small volumes of metal ions. During heat treatment, the dried precursors decompose into nanocrystalline products. The schematic illustration of TNPs' synthesis by using egg white solution is depicted schematically in Figure 1.

3.1. Thermogravimetric Analysis (TGA). Figure 2((a) and (b)) shows the TGA curves of TNPs' sample A and B. According to the curve (a) in Figure 2, sample A experienced two main step downs through the TGA test. The first weight loss happened at about 105°C due to the water evaporation. The second mass loss occurred at 105°C–340°C which is due to the volatilization and combustion of organic species such as CH_3COOH [24]. There is no associated signal with these latter thermal events in the TGA curve confirming the crystallization and phase transition events.

TGA curve of the TNPs synthesized using egg white solution. Sample B is presented in curve (b) of Figure 2. This curve descends until it becomes horizontal around 450°C. TGA curve of sample B experienced three main step downs through the TGA test. The first weight loss between 50 and 110°C is an initial loss of water. The second weight loss starts from 110 to 255°C that is related to the decomposition of the chemically bound and last weigh reduction is between 255 and 450°C due to decomposition of organic groups and albumin. No weight loss between 450 and 900°C was detected on the TGA curve, which indicates the formation of nanocrystalline TiO_2. TGA curve reveals that the proteins were removed by heating process to burn out the organics in air.

3.2. Powder X-Ray Diffraction (XRD). Figure 3((a) and (b)) shows the XRD patterns of samples A and B of TNPs. The XRD peaks in the wide angle range of 2θ ($20° < 2\theta < 90°$) ascertained that the peaks in 25.367°, 37.053°, 37.909°, 38.667°, 48.158°, 54.051°, 55.204°, 62.867°, 68.976°, 70.479°, 75.303°, and 82.926° can be attributed to the 101, 103, 004, 112, 200, 105, 211, 204, 116, 220, 215, and 224 crystalline structures of anatase synthesized TNPs, respectively, (Anatase XRD JCPDS Card no. 78-2486).

The crystallite size (D) can be determined by the Scherrer's formula ($D = K\lambda/(\beta \cos\theta)$). λ is the wavelength of X-ray radiation (CuKα = 0.15406 nm), K is a constant taken as 0.89, β is the line width at half maximum height (FWHM) of the peak, and θ is the diffracting angle. The (101) plane was chosen to calculate the crystalline size (either plane can be used for this purpose). The average crystalline size for the TNPs synthesized with and without using egg white solution is approximately 11 nm to 18 nm, respectively.

3.3. Transmission Electron Microscopy (TEM). TiO_2 nanoparticles were dispersed in distilled water and sonicated ultrasonically. Then, they were dropped cast on a copper grid of TEM. Figures 4(a) and 4(b) show morphology and size distribution of TNPs' samples A and B. The size histograms of the TNPs are shown beside the relative TEM images. The histograms show that the main particle size of samples A and B of TNPs were about 21.45 ± 4.21 nm and 12.55 ± 3.42 nm, respectively.

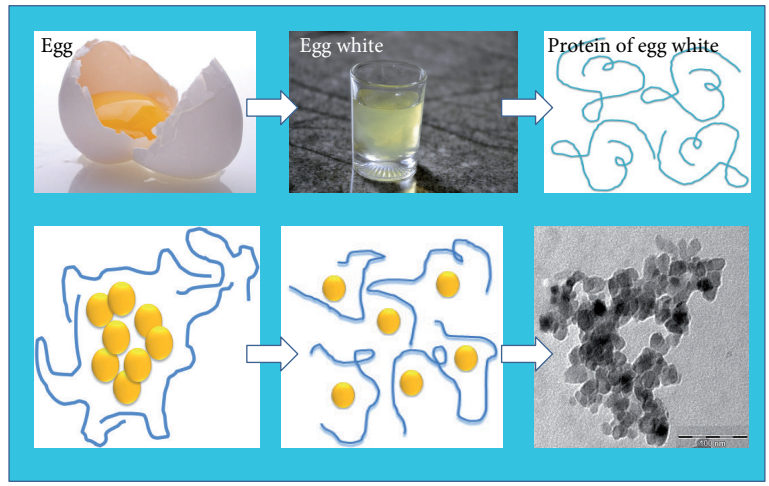

Figure 1: Schematic illustration showing how protein of egg white prevents agglomeration of nanoparticles.

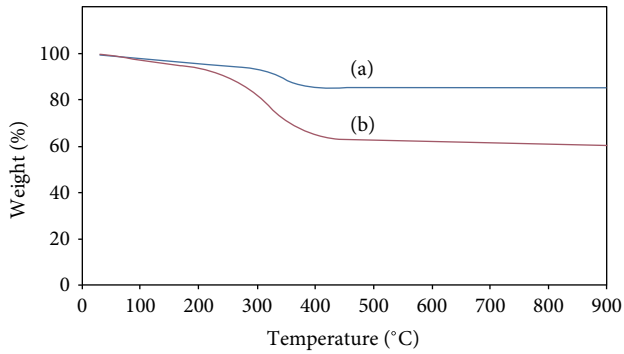

Figure 2: TGA curves for samples A and B of TNPs from room temperature to 900°C ((a) and (b)).

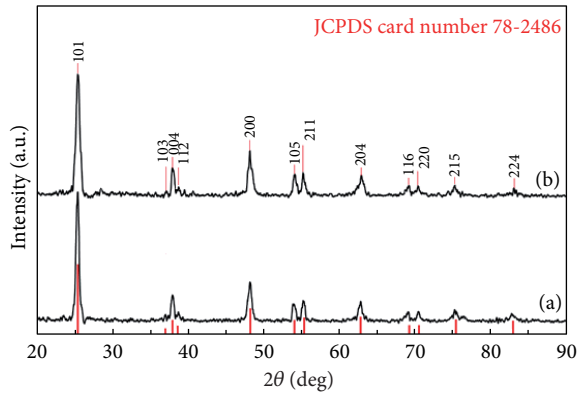

Figure 3: X-ray diffraction patterns for samples A and B of TNPs ((a) and (b)).

3.4. Fourier Transform Infrared Spectroscopy (FTIR). Figure 5((a) and (b)) shows the spectra of TNPs' of samples A and B of which were synthesized via sol-gel method in the range of 400–4000 cm^{-1}. In Figure 5, curve (b) is for sample B of synthesized TNPs by using egg white solution. In this curve, peaks at 485 cm^{-1} and 732 cm^{-1} are for O–Ti–O bonding in anatase morphology [25, 26]. The bands centered at 1621 cm^{-1} and 3354 cm^{-1} are the characteristic of surface-adsorbed water and hydroxyl groups [25]. Curve (a) in Figure 5 shows sample A of TNPs. The peaks at 479 cm^{-1} and 652 cm^{-1} are contributions of the anatase TNPs [27]. The peaks centred at 1627 cm^{-1} at 3388 cm^{-1} are the characteristic of δ-H_2O bending and vibration of hydroxyl groups [26]. There is no peak at 2900 cm^{-1} for curve (a) and (b) of TNPs regarding C–H stretching band, which means all organic compounds were removed from the samples after calcinations.

3.5. UV-Visible Absorption Spectrum. Figure 6((a) and (b)) shows the UV-vis absorption spectra for samples A and B of TNPs between 300 and 800 nm. Sample A has got a peak in 380 nm and sample B has got a peak in 371 nm. It is clear that as the size of particles decreases, peaks become sharper and the absorbance increases in the sample which was synthesized by using egg white solution. The blue shift is ascribed to the decrease in crystallite size.

The band gap energy (E) was calculated as per the literature report [28] using the following equation:

$$\text{Band gap energy } (E) = \frac{hc}{\lambda}, \quad (1)$$

where h is the Planks constant, 6.626×10^{-34} J s, c is the speed of light, 3.0×10^8 m/s and λ is the wavelength (nm). According to this equation the bandgap of sample A is 3.2 eV and the bandpag of sample B is 3.3 eV, and these results confirm that when the size is smaller, the bandgap will be bigger.

A smaller particle size means a larger band gap, since fewer molecular orbitals are being added to the possible energy states of the particle. Hence, absorption will occur at higher energies, so a shift towards shorter wavelengths will be apparent.

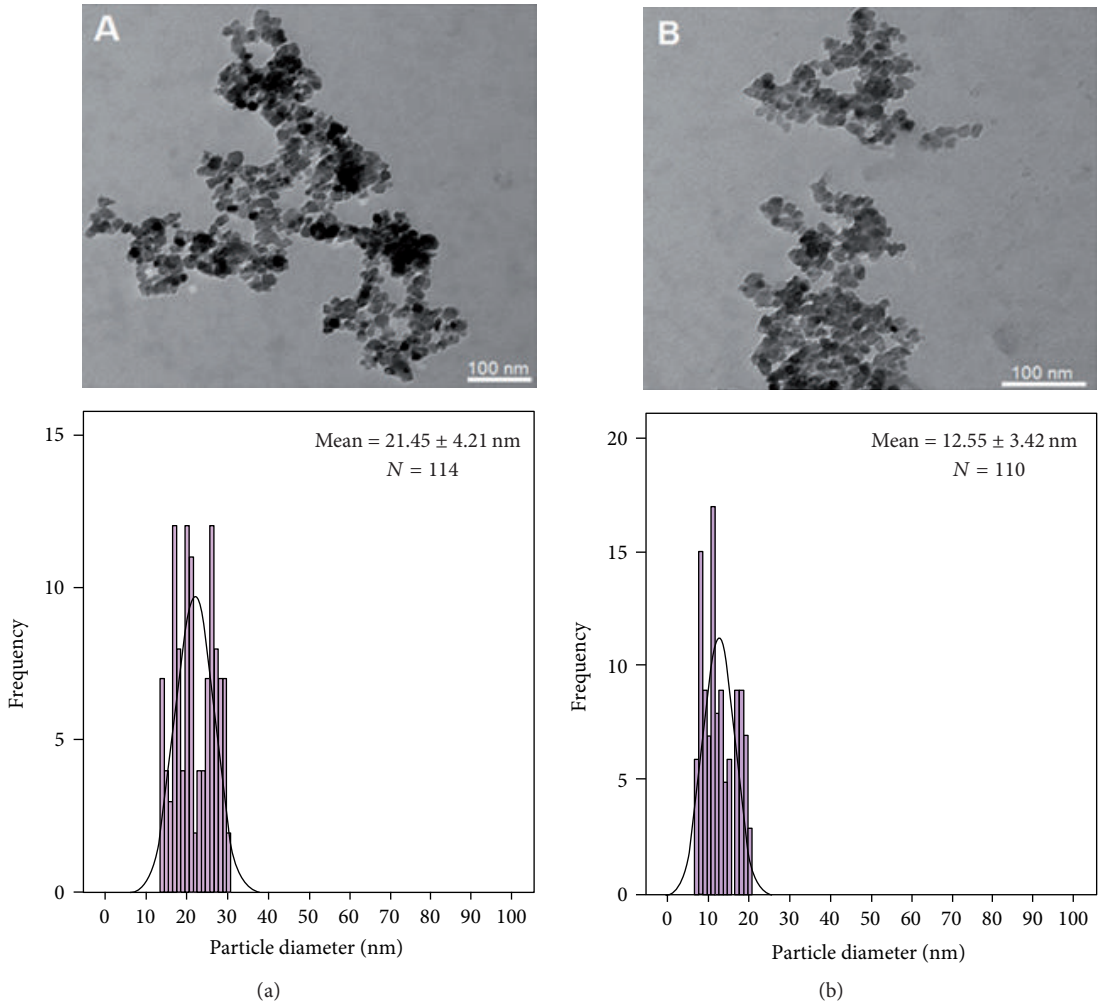

Figure 4: Transmission electron microscopy images and the particle size distributions for samples A and B of TNPs ((a) and (b)).

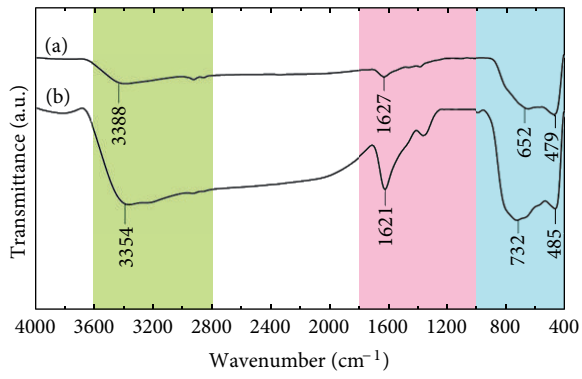

Figure 5: Fourier transform infrared spectra for samples A and B of TNPs ((a) and (b)).

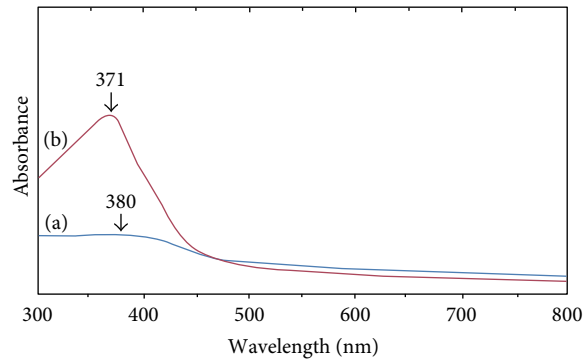

Figure 6: The Ultraviolet visible spectra for samples A and B of TNPs ((a) and (b)).

4. Conclusion

Anatase TNPs were synthesized with and without water-soluble egg white proteins (albumin) by the sol-gel method. From XRD and FTIR results, it is clear that synthesized TNPs exhibited the anatase structure. TEM and XRD results indicate that using egg white solution as a matrix improves the crystallinity and decreases the size of particles. The particle sizes of the TNPs, with and without egg white solution were 12.55±3.42 nm and 21.45±4.21 nm, respectively. Water-soluble proteins of egg white forms a matrix of entangled polymeric chains, inside the cavities of which can trap small

volumes of metal ions. During heat treatment, the dried precursors decompose into nanocrystalline products. The results confirm that egg white solution is an appropriate gelling agent for synthesising TNPs by using sol-gel method. The current simple, cost-effective and environmental friendly synthesis method using water-soluble egg white proteins can be extended to prepare fine particles of other interesting materials.

Acknowledgment

This work was supported by the University of Malaya through Grant no. PV 128/2012A.

References

[1] A. Zaleska, "Doped-TiO_2: a review," *Recent Patents on Engineering*, vol. 2, no. 3, pp. 157–164, 2008.

[2] Y. Xie, Y. Qian, Y. Zhong, H. Guo, and Y. Hu, "Facile low-temperature synthesis of carbon nanotube/TiO_2 nanohybrids with enhanced visible-light-driven photocatalytic activity," *International Journal of Photoenergy*, vol. 2012, Article ID 682138, 6 pages, 2012.

[3] F. Sayilkan, M. Asiltürk, H. Sayilkan, Y. Önal, M. Akarsu, and E. Arpaç, "Characterization of TiO_2 synthesized in alcohol by a sol-gel process: the effects of annealing temperature and acid catalyst," *Turkish Journal of Chemistry*, vol. 29, no. 6, pp. 697–706, 2005.

[4] R. Gómez, T. López, E. Ortiz-Islas et al., "Effect of sulfation on the photoactivity of TiO_2 sol-gel derived catalysts," *Journal of Molecular Catalysis A*, vol. 193, no. 1-2, pp. 217–226, 2003.

[5] U. Yogeswaran and S. M. Chen, "A review on the electrochemical sensors and biosensors composed of nanowires as sensing material," *Sensors*, vol. 8, no. 1, pp. 290–313, 2008.

[6] K. K. Gupta, M. Jassal, and A. K. Agrawal, "Sol-gel derived titanium dioxide finishing of cotton fabric for self cleaning," *Indian Journal of Fibre and Textile Research*, vol. 33, no. 4, pp. 443–450, 2008.

[7] S. Chaturvedi, P. N. Dave, and N. K. Shah, "Applications of nano-catalyst in new era," *Journal of Saudi Chemical Society*, vol. 16, no. 3, pp. 307–325, 2012.

[8] F. Cardarelli, *Materials Handbook: A Concise Desktop Reference*, 2nd edition, 2008.

[9] Z. Liu, Z. Jian, J. Fang, X. Xu, X. Zhu, and S. Wu, "Low-temperature reverse microemulsion synthesis, characterization, and photocatalytic performance of nanocrystalline titanium dioxide," *International Journal of Photoenergy*, vol. 2012, Article ID 702503, 8 pages, 2012.

[10] X. Chen and S. S. Mao, "Titanium dioxide nanomaterials: synthesis, properties, modifications and applications," *Chemical Reviews*, vol. 107, no. 7, pp. 2891–2959, 2007.

[11] M. Lal, V. Chhabra, P. Ayyub, and A. Maitra, "Preparation and characterization of ultrafine TiO_2 particles in reverse micelles by hydrolysis of titanium di-ethylhexyl sulfosuccinate," *Journal of Materials Research*, vol. 13, no. 5, pp. 1249–1254, 1998.

[12] R. R. Basca and M. Gratzel, "Rutile formation in hydrothermally crystallized nanosized titania," *Journal of the American Ceramic Society*, vol. 79, no. 8, pp. 2185–2188, 1996.

[13] T. R. N. Kutty, R. Vivekanandan, and P. Murugaraj, "Precipitation of rutile and anatase (Tio_{12}) fine powders and their conversion to $MTiO_3$ (M = Ba, Sr, Ca) by the hydrothermal method," *Materials Chemistry and Physics*, vol. 19, no. 6, pp. 533–546, 1988.

[14] L. K. Campbell, B. K. Na, and E. I. Ko, "Synthesis and characterization of titania aerogels," *Chemistry of Materials*, vol. 4, no. 6, pp. 1329–1333, 1992.

[15] A. V. Prasada Rao, A. I. Robin, and S. Komarneni, "Bismuth titanate from nanocomposite and sol-gel processes," *Materials Letters*, vol. 28, no. 4–6, pp. 469–473, 1996.

[16] D. F. Vieira and A. Pawlicka, "Optimization of performances of gelatin/$LiBF_4$-based polymer electrolytes by plasticizing effects," *Electrochimica Acta*, vol. 55, no. 4, pp. 1489–1494, 2010.

[17] D. V. Vadehra, K. R. Nath, and R. Forsythe, "Eggs as a source of protein," *CRC Critical Reviews in Food Technology*, vol. 4, no. 2, pp. 193–309, 1973.

[18] E. Li-Chen and S. Nakai, "Biochemical basis for the properties of egg white," *CRC Critical Reviews in Poultry Biology*, vol. 2, no. 1, pp. 21–59, 1989.

[19] Y. Mine, "Recent advances in the understanding of egg white protein functionality," *Trends in Food Science & Technology*, vol. 6, no. 7, pp. 225–232, 1995.

[20] O. Lyckfeldt, J. Brandt, and S. Lesca, "Protein forming—a novel shaping technique for ceramics," *Journal of the European Ceramic Society*, vol. 20, no. 14-15, pp. 2551–2559, 2000.

[21] S. Dhara and P. Bhargava, "Egg white as an environmentally friendly low-cost binder for gelcasting of ceramics," *Journal of the American Ceramic Society*, vol. 84, no. 12, pp. 3048–3050, 2001.

[22] S. Dhara and P. Bhargava, "A simple direct casting route to ceramic foams," *Journal of the American Ceramic Society*, vol. 86, no. 10, pp. 1645–1650, 2003.

[23] S. Doeuff, M. Henry, C. Sanchez, and J. Livage, "Hydrolysis of titanium alkoxides: modification of the molecular precursor by acetic acid," *Journal of Non-Crystalline Solids*, vol. 89, no. 1-2, pp. 206–216, 1987.

[24] R. Parra, M. S. Góes, M. S. Castro, E. Longos, P. R. Bueno, and J. A. Varela, "Reaction pathway to the synthesis of anatase via the chemical modification of titanium isopropoxide with acetic acid," *Chemistry of Materials*, vol. 20, no. 1, pp. 143–150, 2008.

[25] G. Soler-Illia, A. Louis, and C. Sanchez, "Synthesis and characterization of mesostructured titania-based materials through evaporation-induced self-assembly," *Chemistry of Materials*, vol. 14, no. 2, pp. 750–759, 2002.

[26] J. C. Yu, L. Z. Zhang, Z. Zheng, and J. C. Zhao, "Synthesis and characterization of phosphated mesoporous titanium dioxide with high photocatalytic activity," *Chemistry of Materials*, vol. 15, no. 11, pp. 2280–2286, 2003.

[27] K. E. Karakitsou and X. E. Verykios, "Effects of altervalent cation doping of TiO_2 on its performance as a photocatalyst for water cleavage," *Journal of Physical Chemistry*, vol. 97, no. 6, pp. 1184–1189, 1993.

[28] J. Dharma and A. Pisal, UV/Vis/NIR Spectrometer, Perkin Elmer Application Notes.